Available online at www.sciencedirect.com

ScienceDirect

Comput. Methods Appl. Mech. Engrg. 370 (2020) 113268

Computer methods in applied mechanics and engineering

www.elsevier.com/locate/cma

Machine learning of multiscale active force generation models for the efficient simulation of cardiac electromechanics

F. Regazzoni[a,*], L. Dedè[a], A. Quarteroni[a,b]

[a] *MOX - Dipartimento di Matematica, Politecnico di Milano, P.zza Leonardo da Vinci 32, 20133 Milano, Italy*
[b] *Mathematics Institute, École Polytechnique Fédérale de Lausanne (EPFL), Av. Piccard, CH-1015 Lausanne, Switzerland*

Available online 11 July 2020

Abstract

High fidelity (HF) mathematical models describing the generation of active force in the cardiac muscle tissue typically feature a large number of state variables to capture the intrinsically complex underlying subcellular mechanisms. With the aim of drastically reducing the computational burden associated with the numerical solution of these models, we propose a machine learning method that builds a reduced order model (ROM); this is obtained as the best-approximation of the HF model within a class of candidate differential equations based on Artificial Neural Networks (ANNs). Within a semiphysical (gray-box) approach, an ANN learns the dynamics of the HF model from input–output pairs generated by the HF model itself (i.e. non-intrusively), being additionally informed with some a priori knowledge about the HF model. The ANN-based ROM, with just two internal variables, can accurately reproduce the results of the HF model, that instead features more than 2000 variables, under several physiological and pathological working regimes of the cell. We then propose a multiscale 3D cardiac electromechanical model, wherein active force generation is described by means of the previously trained ANN. We achieve a very favorable balance between accuracy of the result (order of 10^{-3} for the main cardiac biomarkers) and computational efficiency (with a speedup of about one order of magnitude), still relying on a biophysically detailed description of the microscopic force generation phenomenon.

© 2020 The Author(s). Published by Elsevier B.V. This is an open access article under the CC BY-NC-ND license (http://creativecommons.org/licenses/by-nc-nd/4.0/).

Keywords: Data-driven modeling; Machine learning; Model Order Reduction; Cardiac simulations; Sarcomere modeling; Artificial Neural Networks

---

1. Introduction

Numerical simulations of the cardiac function require coupling different mathematical models representing processes taking place at different spatial scales [1–5]. Cardiac tissue mechanical activation, which is responsible for the generation of active force and for the contraction of the myocardium, is driven by a subcellular mechanism with characteristic spatial scales of micrometers or less. Hence, when the target is a three-dimensional Finite Element simulation of the heart integrated function [6–9], like for cardiac electromechanics, the mathematical model describing the activation of the cardiac contractile cells should be solved virtually in any point of the computational domain and practically at each nodal point or at every quadrature node of the computational mesh. Since capturing the complexity of realistic heart models requires as many as 10^5–10^6 mesh elements, multiscale numerical

---

[*] Corresponding author.
E-mail address: francesco.regazzoni@polimi.it (F. Regazzoni).

https://doi.org/10.1016/j.cma.2020.113268

0045-7825/© 2020 The Author(s). Published by Elsevier B.V. This is an open access article under the CC BY-NC-ND license (http://creativecommons.org/licenses/by-nc-nd/4.0/).

simulations based on biophysically detailed active contraction models represent a computational challenge, both because of computing time and memory storage. Indeed, due to the intrinsic complexity of the subcellular processes leading to the mechanical activation, it is difficult to build activation models that are at the same time low-dimensional and biophysically accurate [10–12]. This harms the accomplishment of a well balanced trade-off between model computational complexity and model reliability.

In this paper, we propose a multiscale approach to cardiac electromechanics (EM) wherein active force generation at the subcellular level is modeled by a ROM built by means of Artificial Neural Networks (ANNs). We aim at reducing the computational burden associated to the numerical approximation of cardiac EM, wherein complex sarcomere models should be used for accurate simulations. We show, both qualitatively and quantitatively, that our approach and our reduced model realize a very good trade-off between computational efficiency and accuracy.

We build the ANN-based reduced model by further extending the method that we proposed in [13], to which we refer as a black-box machine learning algorithm. The latter, indeed, does not require any knowledge of the high-fidelity (HF) model but only a collection of input–output pairs generated by the HF model. In this work, we move instead towards a gray-box approach (or semi-physical approach), by feeding the ANN learning process with some a priori knowledge on the HF model. We employ this method to reduce the dimensionality and the computational complexity of the cardiac activation model proposed in [14] and we compare the results of simulations performed with the HF and the reduced model.

The paper is organized as follows. In Section 2 we briefly review the mechanism of cardiac force generation and the associated mathematical models, highlighting the difficulties in finding a low dimensional model for this process. Then, we review the available literature on the reduction of computational complexity of activation models. In Section 3 we recall the activation model proposed in [14], which we consider here as the HF model to be reduced and, in Section 4, we present the reduction strategy. In Section 5 we provide the technical details on the ANN training, we show the results obtained, and we validate the ANN-based ROM by means of single cell simulations, under both physiological and pathological conditions. In Section 6 we consider multiscale three-dimensional cardiac EM simulations and we compare the results obtained with the HF activation model and our reduced model. We critically discuss the results obtained in Section 7 and we draw our conclusions in Section 8.

2. Cardiac activation models and model order reduction

The fundamental contractile unit of cardiac muscle tissues is the sarcomere, a cylindrical structure nearly 2 μm long, made of two families of filaments – known as thin and thick filaments – arranged in a highly organized structure [15–20]. Myosin, the principal constituent of thick filaments, is a molecular motor able to bind to actin, which is part of the thin filaments, and to generate force by pulling thin filaments towards the M-line, located at the center of the sarcomere. When the tissue is at rest, however, the regulatory units (i.e. troponin–tropomyosin complexes located on thin filaments) are in a non-permissive configuration that blocks actin binding sites, preventing myosin from generating force [17,18].

Cells contraction is triggered by an increase of the intracellular concentration of calcium ions (that we denote by the variable $[\mathrm{Ca}^{2+}]_{\mathrm{i}}$), which bind to troponin thus making the permissive configuration energetically favorable for the associated regulatory unit. When a regulatory unit is in the permissive configuration, myosin is free to bind to the actin binding sites regulated by that unit, forming the so-called crossbridges and generating active force (see Fig. 1). A regulatory unit acts indeed as a microscopical on–off switch for the generation of force. When calcium concentration returns to its presystolic level, calcium ions detach from troponin and the regulatory units move back to the non-permissive configuration; this sterically hinders the formation of further crossbridges.

Besides calcium concentration, the activation mechanism is regulated by the local stretch of the tissue, which affects the sarcomere length (here denoted by SL). The main consequences of an increment of SL (in the physiological range) are an increase of maximal force at saturating calcium concentrations and an enhanced sensitivity to calcium. This is linked to the Frank–Starling law, for which an increased presystolic volume (at the microscopical level, larger SL) translates into a higher generated force (linked to higher tissue activation at the microscale) [15,16].

Mechanical activation models aim at linking the time evolution of $[\mathrm{Ca}^{2+}]_{\mathrm{i}}(t)$ and of $SL(t)$ (regarded as the two inputs of the model) to the level of activation. The latter is measured by the so-called permissivity – denoted by $y(t) \in [0, 1]$ – that is the fraction of regulatory units in permissive state. When a regulatory unit is in permissive

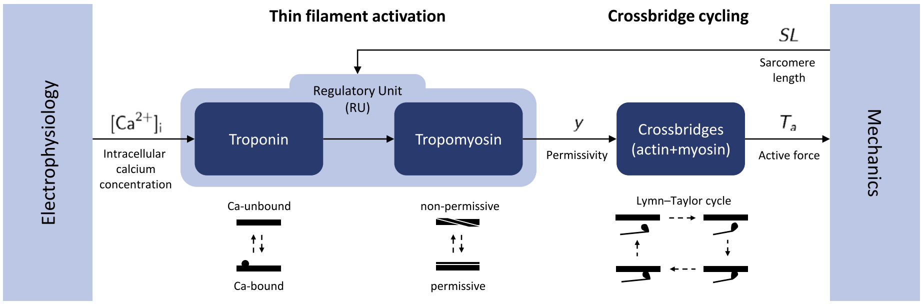

Fig. 1. The cardiac force generation process is split into two parts: first, the regulatory units located on the thin filament (troponin–tropomyosin protein complexes) are activated as a consequence of an increase of intracellular calcium concentration $[\mathrm{Ca}^{2+}]_\mathrm{i}$ and regulated by the sarcomere elongation SL; then, when tropomyosin switches to the permissive configuration, actin and myosin undergo the so-called Lymn–Taylor cycle and generate active force [15].

state, steric hindrance is absent, and force-generating actin–myosin interactions take place. The total active force generated by the muscle tissue is then assumed to be proportional to permissivity [14].

2.1. Modeling cardiac mechanical activation

Mathematical models of cardiac muscle cells activation are typically represented by Continuous-Time Markov Chains describing the transitions of the regulatory units proteins [21–24]. In such stochastic models, a single representative regulatory unit is considered, thus adopting a mean-field approach, to contain computational complexity.

As shown in the seminal contribution of [11], mean-field models are however unable to reproduce the steep nonlinear response of tissue activation to an increase of calcium concentration, which features a Hill coefficient (i.e. a measure of ultrasensitivity of a protein to a ligand, see e.g. [15]) significantly larger than one [25–28]. Indeed, the large Hill coefficient reveals an apparent cooperative behavior between the different units and this cannot be captured by a mean-field model, which considers instead only a single unit. On the contrary, the experimentally observed force–calcium dependence can be recovered by explicitly considering a spatial distribution of regulatory units, which allows to model nearest-neighboring interactions [10].

The drawback of spatially explicit models is their overwhelming computational complexity since the number of degrees of freedom grows exponentially with the number of regulatory units, reaching the order of 10^{21} and even larger [14]. This issue is typically tackled by sampling the solution of spatially-explicit models by the Monte Carlo method, which is however time-consuming and exhibits a slow convergence towards accurate results [11,29–31]. With the Monte Carlo method, a set of possible trajectories of the system, whose state is represented by just a few tens of variables, is simulated and the results are averaged. However, in order to reach statistical convergence, as much as 10^4 trajectories may be required (see e.g. [12,14,31]), raising again the issue of memory storage in three-dimensional realistic cardiac simulations.

Due to their large computational cost, physics-based models of cardiac activation are typically replaced, in large-scale cardiac simulations, by phenomenological models; the latter are empirical relationships obtained by fitting experimental data without being derived from first-principles [32–36]. The reduced computational cost of phenomenological models comes at the price of less mechanistic insight into the multiscale phenomena, the lack of a clear physical interpretation of some of their parameters and a hampered predictive power; the latter drawback mainly comes from the intrinsic difficulties in gathering accurate data on the microscopic phenomena under the working condition of a beating heart. Moreover, unlike for phenomenological models, biophysically detailed models allows to investigate the impact of the macroscopic properties of the contractile apparatus on the macroscopic observable quantities.

2.2. Reducing computational burden of cardiac cells activation models

Due to the abovementioned advantages of physics-based models with respect to phenomenological ones, several attempts have been made to reduce the computational complexity of spatially-explicit models while preserving their reliability, in particular for reproducing the physiological force–calcium relationship [11]. In [10] an exact solution for a spatially-explicit model was proposed, which is however limited to the steady-state. In [37] the large complexity of the proposed reduced model limits its applicability to a small number of regulatory units. In [12] the authors propose an integro-differential system derived from the Forward Kolmogorov Equation associated with the Markov Chain describing the transition of the regulatory units. This system comprises a set of parameters which have to be estimated by a least-squares fitting over a collection of simulations obtained by means of the Monte Carlo method. However, this reduction approach introduces a non-negligible error and the training is performed for specific inputs, without guaranteeing the reliability of the model under different conditions. In [38], aiming at reducing the complexity of a spatially-explicit model, the authors grouped the states of the model by the number of units being in a given state, regardless of their position. Then, the position of units is again taken into account when the transition probabilities are computed by averaging, with Monte Carlo random sampling, over all configurations of the considered group. However, in this model the spatially-explicit description is lost and length dependent effects cannot be captured.

In [14], we introduced a physically motivated assumption of conditionally independence on specific sets of events, which allowed to derive a system of ordinary differential equations (ODEs) for the time evolution of the probability of the states of triplets of consecutive neighboring regulatory units. This model allows to accurately reproduce the results of the original model (with a relative error of order of 10^{-2}) more efficiently than with a Monte Carlo approximation (to get the same error, the latter requires more than 10 000 times of computational time). Moreover, a thorough validation of the model in [14] shows a good qualitative and quantitative agreement with experimental measurements under various settings. In particular, the force–calcium relationship is accurately reproduced, a significantly important achievement for cardiac electromechanics. This model accomplishes a significant reduction of the computational burden, both in terms of model size and of computational time, compared to spatially-explicit models. However, it still features 2176 internal variables, that describe all the possible combinations of triplets of adjacent regulatory units. In a full-organ three-dimensional simulation with a space discretization featuring 10^6 degrees of freedom, the total number of variables associated to the muscle cells activation would be of the order of 10^9. A further significant reduction of the dimensionality of this model is thus desirable, if not necessary. This is precisely our goal in this paper.

2.3. Model order reduction techniques

We consider therefore general purpose Model Order Reduction (MOR) reduction techniques to derive a computationally tractable, lower dimensional counterpart of a HF model, yet accurately reproducing its results [39–41]. MOR techniques can be classified as model-based or data-driven. With the former strategy, the reduced formulation is derived from the HF model, by projecting it onto a smaller space [39,40,42,43]. In this framework, the space of the full-order state is approximated by a lower dimensional subspace, which can be obtained through different techniques, including Moment-Matching [44–46], Balanced-Truncation [43,47] and Proper Orthogonal Decomposition (POD, see [43,48–51]), as in the case of the Reduced Basis (RB) method [41,52]. Projection-based methods are tailored on linear models; if applied to nonlinear models they need to be suitably adapted [41,52–55].

On the other hand, data-driven MOR approaches build the reduced model from a collection of input–output pairs, from which they attempt to infer the dynamics of the HF model. The Loewner framework [56–58] and the orthonormal vector fitting (OVF) method [59,60] are data-driven MOR techniques for linear systems based on an approximation of the transfer function of the HF model in the frequency domain. Data-driven MOR techniques for nonlinear models are, e.g.: dynamic mapping kriging (DMK) [61], which approximates the right-hand side of a nonlinear system by Gaussian Process (GP) regression [62,63]; Sparse Identification of Nonlinear Dynamics (SINDy) [64], which seeks an approximation of the system right-hand side as a combination of a predetermined collection of linear and nonlinear terms; a generalization of the Loewner framework to analytic nonlinear models with affine input dependence [65–67]; Multistep Neural Networks, trained to minimize the residuals of a given multi-step time-stepping scheme on a collection of available snapshots of the full-order state [68]. However, the latter mentioned techniques are aimed to reduce the computational effort of the evaluation of the right-hand side of the HF model and not to reduce its dimensionality. In [69], the authors proposed a MOR technique based on a combination of projection-based methods with GP regression. In [70], an ANN-based MOR method for time-dependent PDEs is proposed. However, the last two methods are restricted to parametric differential equations and cannot be easily extended to models with a time-dependent input.

In [13] we proposed a data-driven MOR technique, based on ANNs, which is suitable for nonlinear models with time-dependent inputs and can provide a significant reduction of dimensionality of the HF model. This approach consists in reformulating the model reduction problem as a maximum-likelihood problem, where one looks for the model which best approximates, inside a class of candidate models, a collection of input–output pairs. Specifically, the set of candidate models consists in systems of ODEs whose right-hand side is represented by an ANN that is trained to learn from the collection of input–output pairs – generated by the HF model – the underlying physics of the HF model itself. We will recall our data-driven MOR technique in Section 4.1 and we will extend it in Section 4.2 by the introduction of suitable penalization terms that enforce some a priori knowledge on the HF model into the learning process.

3. The high fidelity model for cardiac activation

In this work our HF model is the activation model for cardiac muscle cells proposed in [14], describing the time evolution of the probabilities associated to the possible states of triplets of adjacent regulatory units on a myofilament. We have $n_{\mathrm{RU}} = 36$ units, each having 4 possible states given by the combination of the two conditions of being bound to calcium or not and of being in permissive state or not. The transition rates between the states are either directly measured or calibrated from experiments that allow to decouple their effects [10,71]. The cooperative end-to-end iterations among regulatory units are included in the model by thermodynamically consistent nearest-neighboring interactions, as proposed in [10]. Finally, length dependent effects are captured thanks to the spatially-explicit representation of regulatory proteins, that allows to accurately track the filaments overlap.

Since each triplet can be in 4^3 possible states and we have $(n_{\mathrm{RU}} - 2)$ different triplets of adjacent units, the size of the internal state of the model is $N = (n_{\mathrm{RU}} - 2) \cdot 4^3 = 2176$. We denote by $\mathbf{Z}(t) \in \mathbb{R}^N$ the internal state of the HF model, that is the vector collecting all such variables.

The HF model for cardiac activation can be written in the following form:

$$\begin{cases} \dot{\mathbf{Z}}(t) = \mathbf{F}(\mathbf{Z}(t), \mathbf{u}(t)), & t \in (0, T] \\ \mathbf{Z}(0) = \mathbf{Z}_0 \\ y(t) = G(\mathbf{Z}(t)), & t \in (0, T], \end{cases} \tag{1}$$

where the input is given by $\mathbf{u}(t) = ([\mathrm{Ca}^{2+}]_{\mathrm{i}}(t), SL(t))^T$ and the output is the permissivity $y(t)$. The right-hand side $\mathbf{F}$ and the output function G are nonlinear and linear functions, respectively; we refer the interested reader to [14] for the definition of these terms.

Following [10], we assume that each cycling crossbridge can exert a fixed amount of force and that calcium-driven activation represents the rate-limiting step of the force generation dynamics. As the fraction of cycling crossbridges corresponds to the permissivity, the total active tension (T_a) is proportional to y:

$$T_a = \overline{T} y, \tag{2}$$

where $\overline{T}$ is the force generated for $y = 1$. We here neglect shortening velocity-related effects [15,72], which require an explicit representation of crossbridges to be modeled [73–75] and which we will include in a future work.

We remark that whereas in this paper we focus on a specific HF model of active force generation (the one proposed in [14]), the MOR strategy here proposed can be applied to virtually any other HF model of force generation. As a matter of fact in [71] successful examples of application to different active tension models are presented.

4. The model reduction strategy

Within a data-driven framework, we carry out N_s experiments (i.e. numerical simulations) with the HF model and we collect a set of N_s outputs $y(t)$, each one obtained with a different input $\mathbf{u}(t)$. As our goal is to obtain a reduced model to be exploited in multiscale cardiac simulations, our inputs will span the range of values possibly covered during the cardiac activity. In particular, since calcium concentration during each heartbeat varies between 0.1 µM (micromolar) and 1.2 µM and the working range of sarcomeres spans a length from 1.7 µm to 2.3 µm [15,16], our input takes values in $U = [[\mathrm{Ca}^{2+}]_{\mathrm{i,min}}, [\mathrm{Ca}^{2+}]_{\mathrm{i,max}}] \times [SL_{\mathrm{min}}, SL_{\mathrm{max}}]$, where we prudentially set $[\mathrm{Ca}^{2+}]_{\mathrm{i,min}} = 0$ µM, $[\mathrm{Ca}^{2+}]_{\mathrm{i,max}} = 1.5$ µM, $SL_{\mathrm{min}} = 1.6$ µM, $SL_{\mathrm{max}} = 2.4$ µM. Since the output of the model represents the fraction of units in permissive state, we define the space of output values as $Y = [0, 1]$.

We employ the following notation to denote the input–output pairs of the training dataset. For $j = 1, \dots, N_s$, we consider a time interval $[0, T_j]$ and an input function $\widehat{\mathbf{u}}_j : [0, T_j] \to U$ and we define $\widehat{y}_j : [0, T_j] \to Y$ as the solution of the HF model (1) associated to the input $\widehat{\mathbf{u}}_j$. The jth training experiment (where $j = 1, \dots, N_s$) consists of the pair $(\widehat{\mathbf{u}}_j, \widehat{y}_j)$.

The solution of the HF model (1) also depends on the initial condition $\mathbf{Z}_0$. Because of the non-intrusive nature of our approach, a unique initial condition must be used in each experiment, otherwise the input–output map that we aim to learn would not be well-defined (see [13] for more details). Specifically, we set as initial condition for each training experiment the steady-state of the cell in pre-systolic conditions, which is when calcium concentration is $[\mathrm{Ca}^{2+}]_{\mathrm{i},0} = 0.1$ µM and the sarcomere length is $SL_0 = 2.2$ µm. The corresponding state can be numerically computed by solving the HF model with input $\mathbf{u}(t) \equiv \mathbf{u}_0 := ([\mathrm{Ca}^{2+}]_{\mathrm{i},0}, SL_0)^T$, until a steady-state is reached.

4.1. Black-box model reduction

Our ROM will approximate the HF model in the following form:

$$\begin{cases} \dot{\mathbf{z}}(t) = \mathbf{f}(\mathbf{z}(t), \mathbf{u}(t)), & t \in (0, T_j] \\ \mathbf{z}(0) = \mathbf{z}_0 \\ y(t) = \mathbf{z}(t) \cdot \mathbf{e}_1, & t \in (0, T_j], \end{cases} \tag{3}$$

where the reduced state $\mathbf{z}(t)$ belongs to a lower dimensional space $\mathbb{R}^n$ such that $n \ll N$. By setting $y(t) = \mathbf{z}(t) \cdot \mathbf{e}_1$, where $\mathbf{e}_1 = (1, 0, \dots, 0)^T \in \mathbb{R}^n$, we are forcing the first entry of the reduced state to coincide with the output itself. It follows that the first entry of the initial reduced state $\mathbf{z}_0$ (here denoted by $(\mathbf{z}_0)_1$) must coincide with the output associated with the initial full-order state $\mathbf{Z}_0$. Hence, $(\mathbf{z}_0)_1$ represents the presystolic permissivity and is given by $y_0 := G(\mathbf{Z}_0) \simeq 1.5 \cdot 10^{-3}$. As discussed in [13], we can set, without loss of generality, $(\mathbf{z}_0)_i = 0$ for $i = 2, \dots, n$ as this choice does not reduce the set of candidate reduced models (each model not satisfying the condition $(\mathbf{z}_0)_i = 0$ for $i = 2, \dots, n$ can be rewritten, after a change of variables, as a model in the form of Eq. (3) satisfying the aforementioned condition.). To sum up, we set the initial reduced state as $\mathbf{z}_0 = (y_0, 0, \dots, 0)^T$.

By comparing Eq. (1) with Eq. (3), we notice that the full-order state $\mathbf{Z}(t)$ is replaced by a new variable $\mathbf{z}(t)$. Conversely, both the input $\mathbf{u}(t)$ and the output $y(t)$, having the same physical meaning, are denoted with the same symbol. The right-hand side $\mathbf{f}: \mathbb{R}^n \times U \to \mathbb{R}^n$ is the unique element in (3) still to be defined. This term is, in fact, what the machine learning algorithm will learn from the training input–output pairs. Our strategy is that of fixing the dimension n of the ROM, selecting a candidate class of functions $\widehat{\mathcal{F}}$, and interpreting the model reduction problem as a best-approximation problem. In the latter, we look for the function $\mathbf{f} \in \widehat{\mathcal{F}}$ such that the input–output map represented by the model (3) best fits the input–output pairs belonging to the training set. Basically, within all the possible models with n state variables, we are looking for the one which best approximates the HF model. More precisely, we consider the following optimization problem, in which we minimize the distance, in the least-squares sense, between the HF output and the output obtained by the ROM:

$$\begin{cases} \min\limits_{\mathbf{f} \in \widehat{\mathcal{F}}} & \frac{1}{2} \sum_{j=1}^{N_s} \int_0^{T_j} |\widehat{y}_j(t) - y_j(t)|^2 dt \\ \text{s.t.} & \dot{\mathbf{z}}_j(t) = \mathbf{f}(\mathbf{z}_j(t), \widehat{\mathbf{u}}_j(t)), \quad t \in (0, T_j], \quad j = 1, \dots, N_s \\ & \mathbf{z}_j(0) = \mathbf{z}_0, \quad j = 1, \dots, N_s \\ & y_j(t) = \mathbf{z}_j(t) \cdot \mathbf{e}_1, \quad t \in (0, T_j], \quad j = 1, \dots, N_s. \end{cases} \tag{4}$$

The former problem can be interpreted as a maximum-likelihood problem, where the unknown is $\mathbf{f} \in \widehat{\mathcal{F}}$, subject to the constraint given by the model itself. Clearly, we need to suitably select the set of candidate functions $\widehat{\mathcal{F}}$. Because of their universal approximation properties [76] and their well assessed ability of learning manifolds from data [77,78], we set as candidate functions space $\widehat{\mathcal{F}}$ the space of functions represented by ANNs with a prescribed architecture. ANNs are functions from $\mathbb{R}^p$ to $\mathbb{R}^q$ (in our case, $p = n + 2$ and $q = n$), parametrized by a finite number of parameters (representing the weights and biases), which are collected in a real valued vector $\boldsymbol{\mu} \in \mathbb{R}^k$, for $k \geq 1$ (see e.g. [79]). To stress the dependence of $\mathbf{f}$ on the parameters $\boldsymbol{\mu}$, we will use henceforth the notation $\mathbf{f}(\mathbf{z}, \mathbf{u}; \boldsymbol{\mu})$. We remark that the use of ANNs as space of candidate functions has a solid theoretical basis since, as we proved in [13], any time-dependent differential equation can be approximated with arbitrary accuracy by an ANN-based model.

In this manner, problem (4) can be written as an optimization problem in $\mathbb{R}^k$ and standard optimization techniques can be employed for its solution. In particular, we use the Levenberg–Marquardt algorithm [80], an approximated Newton method, specifically designed for least-squares problems, that exploits first-order derivative information to approximate the second-order derivatives. For the computation of the gradients of the least-squares terms with respect to the design variables $\boldsymbol{\mu}$, an adjoint backward equation is solved at each iteration of the optimization algorithm. We refer the interested reader to [13] for the technical details.

4.2. *Feeding the learning process with a priori knowledge*

The approach presented so far is fully black-box, that is it does not require any knowledge about the HF model except for a collection of input–output pairs generated by the HF model itself. However, as for the application considered in this paper, we may actually have some insight into the HF model that we aim to reduce. Such a priori knowledge can be exploited in the learning process by adding to the cost functional of problem (4) suitable penalization terms, that we introduce in this section.

4.2.1. *The cycle condition*

As explained in [13], with the proposed approach it is not possible to give a physical meaning to all the entries of the reduced state $\mathbf{z}(t)$, apart from $(\mathbf{z}(t))_1$, which coincides with the permissivity y. This is intimately linked with the black-box nature of data-driven approaches. Nonetheless, the reduced state $\mathbf{z}$ is a compact representation of the full-order state $\mathbf{Z}$: we may suppose that there exists a map between the full-order and the reduced state. Hence, the initial state $\mathbf{Z}_0$ is mapped, by construction, into the reduced initial state $\mathbf{z}_0$.

This implies that, whenever the HF model returns to the initial state at the final time T_j, i.e., $\mathbf{Z}(T_j) = \mathbf{Z}_0$, the ROM should correspondingly satisfy $\mathbf{z}(T_j) = \mathbf{z}_0$. To enforce this condition, which we call *cycle condition*, we insert in the training set some experiments, labeled by the indexes $j \in J_r$, such that at final time T_j the full-order state coincides with the initial state $\mathbf{Z}_0$. Then, we add to the cost functional of problem (4) the following term:

$$E_{\mathrm{c}}^2 = a_{\mathrm{c}}^{-1} \sum_{j \in J_r} \sum_{i=2}^{n} \frac{\left(\mathbf{z}_j(T_j) \cdot \mathbf{e}_i\right)^2}{\frac{1}{T_j} \int_0^{T_j} \left(\mathbf{z}_j(t) \cdot \mathbf{e}_i\right)^2 \, \mathrm{d}t}, \tag{5}$$

where $a_{\mathrm{c}} = |J_r|(n-1)$ is a normalization factor, whose role will be discussed later. We remark that E_{c} does not involve $(\mathbf{z})_1$ since it is already accounted for in the cost functional of problem (4). We also notice that in (5) we normalize with respect to the L^2 norm of the history of $\mathbf{z}(t)$, otherwise the introduction of the penalization term (5) would be useless. Indeed, by performing a change of variable the internal state by multiplying its entries, but for the first one, by a small constant $\alpha \ll 1$, the quantity $\sum_{j \in J_r} \sum_{i=2}^{n} \left(\mathbf{z}_j(T_j) \cdot \mathbf{e}_i\right)^2$ can be made arbitrary small, without changing the input–output map represented by the model.

4.2.2. *The equilibrium condition*

In Section 4 we have defined the initial full-order state $\mathbf{Z}_0$ as the steady-state associated to the input $\mathbf{u}_0$. Therefore, such state is by definition an equilibrium solution (i.e. $\mathbf{F}(\mathbf{Z}_0, \mathbf{u}_0) = \mathbf{0}$), a condition that should be satisfied also by the ROM (i.e. $\mathbf{f}(\mathbf{z}_0, \mathbf{u}_0) = \mathbf{0}$). To enforce this condition (which we call *equilibrium condition*), we envisage two alternative strategies. The first one, which we call *weak imposition*, consists in adding to the cost functional the following further penalization term:

$$E_{\mathrm{e}}^2 = a_{\mathrm{e}}^{-1} |\mathbf{f}(\mathbf{z}_0, \mathbf{u}_0)|^2, \tag{6}$$

where the normalization factor is defined as $a_{\mathrm{e}} = n$. The second one consists in manipulating the ANN architecture in such a way that the equilibrium condition is exactly satisfied. Specifically, we redefine $\mathbf{f}$ as $\mathbf{f}(\mathbf{z}, \mathbf{u}) = \bar{\mathbf{f}}(\mathbf{z}, \mathbf{u}) -$

$\bar{\mathbf{f}}(\mathbf{z}_0, \mathbf{u}_0)$, where $\bar{\mathbf{f}}$ stands as the ANN to be trained (from which we remove the last layer of biases since it is canceled by the subtraction). We call this second approach *strong imposition* of the equilibrium condition as the latter is satisfied by construction. In other words, we train the ANN weights and biases, excluding the biases of the output layer, which are defined in such a way that the equilibrium condition is satisfied. The reduction of the number of the unknowns is a consequence of the reduction of the space of candidate solutions (we have excluded the functions not satisfying the equilibrium condition).

4.3. Gray-box model reduction

The introduction of the cycle condition and of the equilibrium condition, made in Section 4.2, would not be possible in a strict black-box framework since the internal state would not be observable. We have thus moved towards a gray-box approach since we have mixed a black-box technique with some insight on the HF model. Before stating the formulation of the gray-box model reduction problem, we introduce the following notation to denote the cost-functional of the black-box formulation (4), which penalizes the error between the HF model and the ROM

$$E_{\mathrm{b}}^2 = a_{\mathrm{b}}^{-1} \sum_{j=1}^{N_s} \int_0^{T_j} |\widehat{y}_j(t) - y_j(t)|^2 dt, \tag{7}$$

where $a_{\mathrm{b}} = \sum_{j=1}^{N_s} \int_0^{T_j} |\widehat{y}_j(t)|^2 dt$. Then, the gray-box MOR problem reads:

$$\begin{cases} \min\limits_{\boldsymbol{\mu} \in \mathbb{R}^k} & \frac{1}{2} w_{\mathrm{b}}^2 E_{\mathrm{b}}^2 + \frac{1}{2} w_{\mathrm{c}}^2 E_{\mathrm{c}}^2 + \frac{1}{2} w_{\mathrm{e}}^2 E_{\mathrm{e}}^2 \\ \text{s.t.} & \dot{\mathbf{z}}_j(t) = \mathbf{f}(\mathbf{z}_j(t), \widehat{\mathbf{u}}_j(t); \boldsymbol{\mu}), \quad t \in (0, T_j], \quad j = 1, \dots, N_s \\ & \mathbf{z}_j(0) = \mathbf{z}_0, \quad j = 1, \dots, N_s \\ & y_j(t) = \mathbf{z}_j(t) \cdot \mathbf{e}_1, \quad t \in (0, T_j], \quad j = 1, \dots, N_s. \end{cases} \tag{8}$$

The weight factors $w_{\mathrm{b}}, w_{\mathrm{c}}, w_{\mathrm{e}} \in \mathbb{R}^+$ allow to tune the contribution of the different terms. The normalization factors a_{b}, a_{c} and a_{e} allow to keep the relative weight of the different terms unaffected by changes in the number of training samples, in J_r or in n. When the strong imposition of the equilibrium condition is employed, we set $w_{\mathrm{e}} = 0$ and we modify the architecture of $\mathbf{f}$ accordingly.

4.4. Discrete version of the MOR problem

We discretize in the problem (8) both for the state equation and the objective functional. As in [13], we consider uniform subdivisions of the time intervals $[0, T_j]$ with step-size Δt; then, we discretize the state equation by a Forward Euler scheme and the objective functional in (8) by the composite trapezoidal rule [81].

We notice that all the terms of the objective functional of problem (8) can be written as sum of squares. The optimization problem retains a least-squares structure and the Levenberg–Marquardt algorithm can thus be applied. The unique change with respect to the solution of the fully black-box problem (4) is that it requires the calculation of the gradient of the terms E_{c} and E_{e} with respect to the design variables $\boldsymbol{\mu}$. Such gradients can be obtained by means of the Lagrange Multiplier method (as in [13]) and by differentiation with respect to $\boldsymbol{\mu}$, respectively.

5. The reduced cardiac activation model

In this section, we provide details on the ANN training and we present our strategy to select the hyperparameters (i.e. the ANN architecture, the weights of the physics-based penalization terms and the strategy used to impose the equilibrium condition). Then, we show the results obtained with the selected ROM, by validating it against experimental data, under physiological and pathological conditions.

5.1. Training the ANN

To train the ANN we generate a training set by means of the HF model, i.e. a collection of input–output pairs $(\widehat{\mathbf{u}}_j, \widehat{y}_j)$, for $j = 1, \dots, N_s$. In such training set we insert three kinds of input functions:

- 50 step responses of duration $T = 3$ s, in the form of $\mathbf{u}(t) = \mathbf{u}_0 + (\bar{\mathbf{u}} - \mathbf{u}_0)\mathbb{1}_{[t_1,t_2)}(t)$, where $t_1 = 0.2$ s, $t_2 = 2$ s and where $\bar{\mathbf{u}}$ is randomly selected, being $\mathbb{1}_A$ the indicator function of the set A. Specifically, we put into the train set 40 inputs where the values $\bar{\mathbf{u}}$ are selected by Latin Hypercube Sampling (LHS) of the input set U and 10 additional inputs obtained by LHS of the subset $[0.3, 0.6]$ μM × $[2.15, 2.25]$ μm $\subset U$. In the latter region, indeed, the steady-state force–length relationship has a non regular shape and thus requires a better resolution to be appreciated. The samples belonging to this set are such that the final full state $\mathbf{Z}(T)$ virtually coincides (with a relative error lower that 10^{-4}) with $\mathbf{Z}_0$. Therefore, we set the corresponding indexes into the set J_r.
- 45 oscillating inputs of duration $T = 1$ s, in the form of $\mathbf{u}(t) = ([\mathrm{Ca}^{2+}]_{\mathrm{i,min}} + A\sin(\frac{2\pi}{T_1}t)^2, B + C\sin(\frac{2\pi}{T_2}t))^T$, where the periods T_1 and T_2 are randomly selected in the range $0.1 - 0.8$ s and the constants A, B and C are randomly selected, with the constrain that the function values belong to the set U.
- 60 randomly generated inputs of duration $T = 1$ s.

For selecting the hyperparameters, we proceed by a trial-and-error approach. Aiming at a drastic reduction of dimensionality of the HF model, we set $n = 2$ internal variables for the ROM. For this choice we found that two hidden layers of 6 neurons each yield accurate results without a significant overfitting, as we will show later (Table 1). Concerning the weights of the loss function, we set, without loss of generality, $w_{\mathrm{b}} = 1$; indeed the learning process is only affected by the ratio of the weights. For all the results of this paper, we set $w_{\mathrm{c}} = 10^{-1}$ and (in the case of weak imposition of the equilibrium condition) $w_{\mathrm{e}} = 10^{-1}$. This choice is driven by a compromise between the satisfaction of the physics-based constraints and the minimization of the data-driven loss function. However, our experience indicates that the learning outcome is not sensibly affected by the choice of w_{c} and w_{e}, unless much larger or smaller values are employed.

To evaluate the accuracy of the ROM, we build a testing set with a collection of step inputs, randomly generated inputs and the physiological and pathological inputs described in Section 5.2. Moreover, in order to evaluate the reliability of the ROM over time intervals longer than the one used for the training, we also test the ROM with random inputs of duration $T = 10$ s.

Therefore, the ANN is trained based on the input–output pairs generated by the HF model under fundamental regimes (step responses, frequency responses) and random inputs. Then, the learned model is tested on different test cases, including physiological samples. If the ANN model, which has been exposed during the training stage only to fundamental inputs, is able to reproduce the results of the HF model also for physiological inputs, we can conclude that the ANN has really *learned* the dynamics of the system, and it is not simply interpolating between a database of precomputed solutions.

In Table 1 we compare the training and testing errors obtained with and without imposition of the equilibrium condition (in weak or strong form) and with or without imposition of the cycle condition. We conclude that the best strategy consists in introducing in the learning process both the cycle condition and the equilibrium condition (the latter with strong imposition). All the results shown in the rest of this paper have been obtained with the ANN model built by means of the aforementioned strategy. For simplicity, we will refer to this model as *the ANN model*. The trained ANN is publicly available online (see Appendix A).

5.2. Validation of the reduced model

We perform with the HF and the ANN models some of test cases typically employed to validate microscopic cardiac force generation models and we check that the ANN model did not lose the capability of the HF model to reproduce the experimentally observed features of cardiac force generation. The results, reported in Fig. 2 and briefly commented in the next sections, show a remarkably good match.

5.2.1. Steady-state force–calcium–length relationships

An important characterization of muscle tissue models is the dependence of the steady-state force on the two inputs, $[\mathrm{Ca}^{2+}]_{\mathrm{i}}$ and SL (see Figs. 2a and 2b respectively). The force–calcium relationship reveals the characteristic

Table 1
Training and testing relative errors obtained by training the ANN model with or without imposition of the equilibrium condition (in either weak or strong form) and with or without imposition of the cycle condition.

Equilibrium condition	Cycle condition	Train error	Test error
–	–	1.62×10^{-2}	2.66×10^{-2}
Weak ($w_e = 10^{-1}$)	–	1.52×10^{-2}	2.10×10^{-2}
Strong	–	1.70×10^{-2}	3.10×10^{-2}
Weak ($w_e = 10^{-1}$)	$w_c = 10^{-1}$	1.48×10^{-2}	2.35×10^{-2}
Strong	$w_c = 10^{-1}$	1.44×10^{-2}	1.97×10^{-2}

sigmoidal shape, with a steep slope in proximity of half activation. An increase in SL leads to an increase of plateau force and to an increase of calcium sensitivity, which translates in a leftward shift of the curve. Conversely, the force–length relationship features increasing curves for $SL < 2.2$ µm, with a change of convexity as $[\mathrm{Ca}^{2+}]_\mathrm{i}$ increases (from convex to concave), and a plateau for $SL > 2.2$ µm (see e.g. [26–28]).

5.2.2. Isometric twitches

Then, we consider isometric twitches, i.e. force transients in response to the calcium wave occurring at each heartbeat, at constant SL. We impose the following calcium transient (from [12]):

$$[\mathrm{Ca}^{2+}]_\mathrm{i}(t) = [\mathrm{Ca}^{2+}]_{\mathrm{i},0} + \frac{[\mathrm{Ca}^{2+}]_{\mathrm{i,peak}} - [\mathrm{Ca}^{2+}]_{\mathrm{i},0}}{\beta} \left[e^{-\frac{t-t_0}{\tau_1}} - e^{-\frac{t-t_0}{\tau_2}} \right] \mathbb{1}_{t \geq t_0}, \tag{9}$$

where

$$\beta = \left(\frac{\tau_1}{\tau_2}\right)^{-\left(\frac{\tau_1}{\tau_2}-1\right)^{-1}} - \left(\frac{\tau_1}{\tau_2}\right)^{-\left(1-\frac{\tau_2}{\tau_1}\right)^{-1}}$$

and $[\mathrm{Ca}^{2+}]_{\mathrm{i},0} = 0.1$ µM, $t_0 = 0.1$ s, $\tau_1 = 0.02$ s, $\tau_2 = 0.11$ s. In Fig. 2c, we set $[\mathrm{Ca}^{2+}]_{\mathrm{i,peak}} = 1.2$ µM and we consider different values of SL. Conversely, in Fig. 2d, we set $SL = 2$ µm and we let $[\mathrm{Ca}^{2+}]_{\mathrm{i,peak}}$ vary. In both cases, by increasing either $[\mathrm{Ca}^{2+}]_{\mathrm{i,peak}}$ or SL, three effects can be observed: (1) the peak force increases; (2) the activation time is not significantly affected; (3) the relaxation time increases (see e.g. [82,83]).

5.2.3. Sudden development of tension

Experiments show that the rate of tension development following a sudden rise of $[\mathrm{Ca}^{2+}]_\mathrm{i}$, starting from its presystolic value of near 0.1 µM, increases with the calcium level [84–87]. To replicate this phenomenon, we apply a step change in calcium at different levels, with $SL = 2.2$ µm. The results are shown in Fig. 2e.

5.2.4. Isometric versus shortening twitches

The systolic contraction of the myocardium leads to a shortening of the muscle fibers and, as a consequence, to a decrease of SL. Therefore, in the normal cardiac activity, shortening twitches, rather than isometric twitches, are observed. To investigate the difference between the two settings, we consider the experimentally measured $[\mathrm{Ca}^{2+}]_\mathrm{i}$ and SL transients reported in [88]. The results of the simulation, shown in Fig. 2f, show that the decrease of SL leads to a decrease of force peak and to a slight decrease of duration of activation (see e.g. [15,16]).

5.2.5. Long-term twitches

The normal cardiac activity features a nearly periodic behavior. To test the capability of our model to sustain a periodic input after several cycles, we perform 10 s long simulations by applying the calcium transient (9), with $[\mathrm{Ca}^{2+}]_{\mathrm{i,peak}} = 1.1$ µM and $SL = 2$ µm, with different periods, ranging from 0.3 to 1.5 s (see Fig. 2g). We notice that for the highest frequency the *wave summation* phenomenon occurs, by which the effect of consecutive twitches sums up in a sustained contraction state (see e.g. [15,16]).

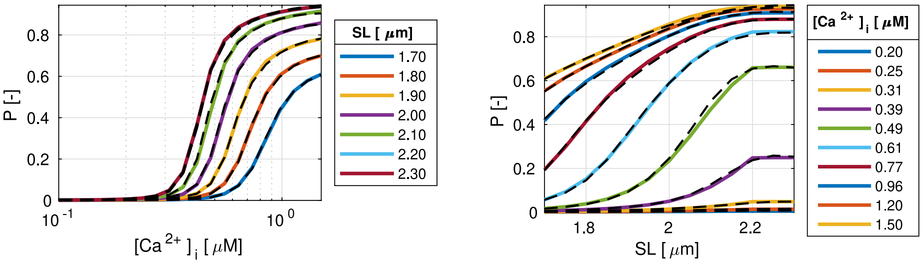

(a) Steady-state force-calcium relationship at different SL

(b) Steady-state force-length relationship at different $[Ca^{2+}]_i$

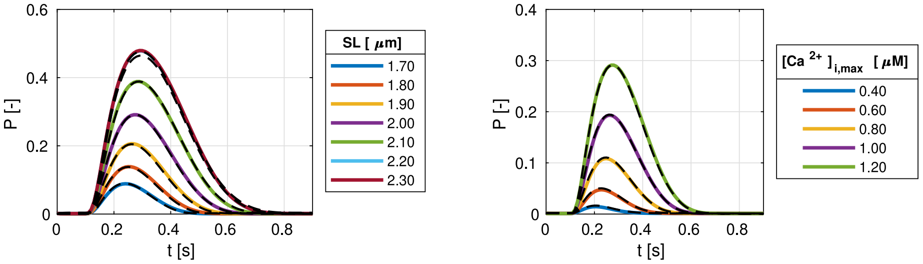

(c) Isometric twitches at different SL

(d) Isometric twitches with different $[Ca^{2+}]_i$ peaks

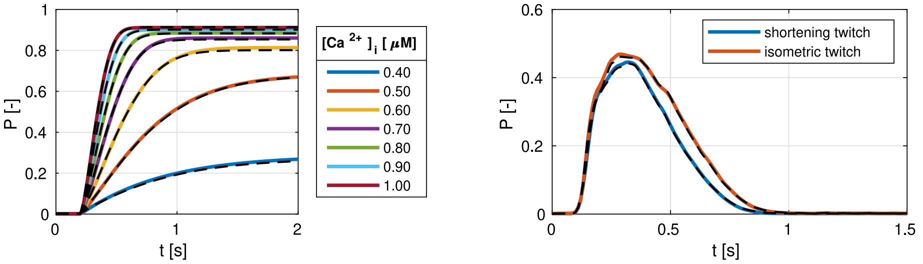

(e) Tesion development for different $[Ca^{2+}]_i$ steps

(f) Experimentally measured twitches (from [88])

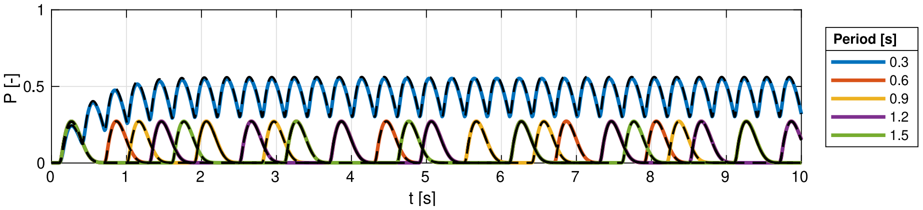

(g) Long-term response to periodic twitches at different frequencies

Fig. 2. Comparison between the results of the HF model (colored solid lines) and the ANN-based reduced model (black dashed lines) for different test cases, discussed in Section 5.2. (For interpretation of the references to color in this figure legend, the reader is referred to the web version of this article.)

6. Three dimensional cardiac electromechanics

We present our approach to reduce the computational burden associated to the numerical approximation of multiscale cardiac EM, where we describe force generation at the microscopic level by means of the reduced ANN model developed in Section 5. First, we introduce the EM problem (Section 6.1) and its numerical discretization (Section 6.2). Then, we illustrate our multiscale strategy (Section 6.3) and we assess the results, both in terms of efficiency and accuracy with three test cases (Sections 6.4 and 6.5).

6.1. The EM problem

We consider a reference computational domain Ω_0, representing the left ventricle (LV) muscle tissue, and a final time $T = 0.8$ s (the characteristic duration of a heartbeat). We define the following functions, defined over the space–time domain $\Omega_0 \times [0, T]$ (in the following the dependence on $(\mathbf{x}, T)$ will be implicit): the transmembrane potential v, the ionic variables $\mathbf{w}$, the activation variables $\mathbf{Z}$ and the displacement $\mathbf{d}$. By using a standard notation, we denote by $\mathbf{F} = \mathbf{I} + \nabla \mathbf{d}$ the deformation gradient in the reference configuration and by $J = \det \mathbf{F}$ its Jacobian. To account for the anisotropic properties of the cardiac tissue, we define a local frame of reference by means of the mutually orthogonal vector fields $\mathbf{f}_0$, $\mathbf{s}_0$ and $\mathbf{n}_0$, denoting respectively the fibers direction, the sheets directions and a direction normal to the previous ones [89].

6.1.1. Electrophysiology

To model the propagation of the action potential, we consider the monodomain equation, which reads (see e.g. [90,91]):

$$\begin{cases} \chi_m \left(C_m \dfrac{\partial v}{\partial t} + \mathcal{I}^{\text{ion}}(v, \mathbf{w}) \right) = \nabla \cdot \left(J\, \mathbf{F}^{-1} \mathbf{D}_m \mathbf{F}^{-T} \nabla v \right) + \mathcal{I}^{\text{app}} & \text{in } \Omega_0 \times (0, T] \\ \dfrac{\partial \mathbf{w}}{\partial t} = \mathbf{h}(v, \mathbf{w}) & \text{in } \Omega_0 \times (0, T] \\ \left(J\, \mathbf{F}^{-1} \mathbf{D}_m \mathbf{F}^{-T} \nabla v \right) \cdot \mathbf{N} = 0 & \text{on } \partial\Omega_0 \times (0, T] \\ v = v_0, \quad \mathbf{w} = \mathbf{w}_0 & \text{in } \Omega_0 \times \{0\}, \end{cases} \tag{10}$$

where $\mathbf{N}$ denotes the outer normal versor at the surface. The functions $\mathcal{I}^{\text{ion}}$ and $\mathbf{h}$ are specified according to the ionic model. In this work we consider the ten Tusscher–Panfilov model with 18 variables in the M cells setting [92]. To reduce the number of parameters, we divide the first equation by the membrane surface to volume ratio χ_m and by the membrane capacitance C_m, obtaining:

$$\frac{\partial v}{\partial t} + \widetilde{\mathcal{I}}^{\text{ion}}(v, \mathbf{w}) = \nabla \cdot \left(J\, \mathbf{F}^{-1} \widetilde{\mathbf{D}}_m \mathbf{F}^{-T} \nabla v \right) + \widetilde{\mathcal{I}}^{\text{app}}$$

where $\widetilde{\mathcal{I}}^{\text{ion}} = C_m^{-1} \mathcal{I}^{\text{ion}}$, $\widetilde{\mathcal{I}}^{\text{app}} = C_m^{-1} \chi_m^{-1} \mathcal{I}^{\text{app}}$ and $\widetilde{\mathbf{D}}_m = C_m^{-1} \chi_m^{-1} \mathbf{D}_m$. To account for the anisotropic properties of the tissue, we write the diffusion tensor as $\widetilde{\mathbf{D}}_m = \sigma_{\text{iso}}(\mathbf{I} - \mathbf{f}_0 \otimes \mathbf{f}_0) + \sigma_{\text{f}}\, \mathbf{f}_0 \otimes \mathbf{f}_0$. The electrical signal is triggered by the applied current $\widetilde{\mathcal{I}}^{\text{app}}$. In this work, we do not explicitly model the Purkinje network and consider instead a collection of points $\mathbf{x}_1, \dots, \mathbf{x}_{N_p}$ where the electrical stimulus is applied, yielding

$$\widetilde{\mathcal{I}}^{\text{app}}(\mathbf{x}, t) = \mathcal{I}^{\max} \sum_{j=1}^{N_p} \exp\left(\frac{|\mathbf{x} - \mathbf{x}_j|^2}{\delta^2} \right) \mathbb{1}_{[0, t_{\text{app}}]}(t).$$

6.1.2. Cardiac tissue activation

Among the ionic variables of the ten Tusscher–Panfilov model, there is the intracellular calcium concentration. To recover the other input variable of the cardiac activation model proposed in [14], namely the local sarcomere length SL, we assume that the sarcomere deformation is proportional to the local deformation in the fiber direction, i.e. $SL = SL_0 \sqrt{\mathcal{I}_{4,f}}$, where $\mathcal{I}_{4,f} = \mathbf{F}\mathbf{f}_0 \cdot \mathbf{F}\mathbf{f}_0$. To regularize the $\mathcal{I}_{4,f}$ field, which may be irregular, especially on coarse FEM computational meshes, we define SL as solution of the following differential problem:

$$\begin{cases} \left(SL - SL_0 \sqrt{\mathcal{I}_{4,f}} \right) - \delta_{SL}^2 \Delta SL = 0 & \text{in } \Omega_0 \times (0, T] \\ \delta_{SL}^2 \nabla SL \cdot \mathbf{N} = 0 & \text{on } \partial\Omega_0 \times (0, T] \end{cases} \tag{11}$$

where δ_{SL} is the regularization parameter. Then, the activation equation, by employing the model proposed in [14], reads:

$$\begin{cases} \dfrac{\partial \mathbf{Z}}{\partial t} = \mathbf{F}(\mathbf{Z}, ([\text{Ca}^{2+}]_{\text{i}}, SL)^T) & \text{in } \Omega_0 \times (0, T] \\ \mathbf{Z}(0) = \mathbf{Z}_0 & \text{in } \Omega_0 \times \{0\}. \end{cases} \tag{12}$$

The active tension field is then computed as $T_a = \overline{T}\, G(\mathbf{Z})$

6.1.3. Mechanics

The balance of momentum written in the reference domain reads as follows (see e.g. [93]):

$$\begin{cases} \rho \dfrac{\partial^2 \mathbf{d}}{\partial t^2} - \nabla \cdot \mathbf{P}(\mathbf{d}) = \mathbf{0} & \text{in } \Omega_0 \times (0,T] \\ \mathbf{P}(\mathbf{d})\mathbf{N} + (\mathbf{N} \otimes \mathbf{N}) \left(K_{\perp}^{\mathrm{epi}} \mathbf{d} + C_{\perp}^{\mathrm{epi}} \dfrac{\partial \mathbf{d}}{\partial t} \right) & \\ \qquad + (\mathbf{I} - \mathbf{N} \otimes \mathbf{N}) \left(K_{\parallel}^{\mathrm{epi}} \mathbf{d} + C_{\parallel}^{\mathrm{epi}} \dfrac{\partial \mathbf{d}}{\partial t} \right) = \mathbf{0} & \text{on } \Gamma_0^{\mathrm{epi}} \times (0,T] \\ \mathbf{P}(\mathbf{d})\mathbf{N} = \dfrac{\| J \mathbf{F}^{-T} \mathbf{N} \|}{\int_{\Gamma_0^{\mathrm{base}}} \| J \mathbf{F}^{-T} \mathbf{N} \| d\Gamma_0} \displaystyle\int_{\Gamma_0^{\mathrm{endo}}} p J \mathbf{F}^{-T} \mathbf{N} d\Gamma_0 & \text{on } \Gamma_0^{\mathrm{base}} \times (0,T] \\ \mathbf{P}(\mathbf{d})\mathbf{N} = -p J \mathbf{F}^{-T} \mathbf{N} & \text{on } \Gamma_0^{\mathrm{endo}} \times (0,T] \\ \mathbf{d} = \mathbf{d}_0, \quad \dfrac{\partial \mathbf{d}}{\partial t} = \dot{\mathbf{d}}_0 & \text{in } \Omega_0 \times \{0\}, \end{cases} \tag{13}$$

where the total Piola–Kirchhoff stress tensor $\mathbf{P}$ is split, by adopting an active stress approach [94], into a passive and an active contribution as $\mathbf{P} = \mathbf{P}^{\mathrm{pass}} + \mathbf{P}^{\mathrm{act}}$. The passive term is defined as the differential of the hyperelastic energy $\mathcal{W}$ with respect to the deformation gradient ($\mathbf{P}^{\mathrm{pass}} = \frac{\partial \mathcal{W}}{\partial \mathbf{F}}$). We consider a quasi-incompressible exponential material model [95] with the hyperelastic energy defined by

$$\begin{aligned} \mathcal{W} &= \frac{C}{2} \left(e^{Q} - 1 \right) + \frac{B}{2} (J-1) \log J \\ Q &= b_{ff} E_{ff}^2 + b_{ss} E_{ss}^2 + b_{nn} E_{nn}^2 \\ &\quad + b_{fs} \left(E_{fs}^2 + E_{sf}^2 \right) + b_{fn} \left(E_{fn}^2 + E_{nf}^2 \right) + b_{sn} \left(E_{sn}^2 + E_{ns}^2 \right), \end{aligned} \tag{14}$$

where $E_{ab} = \mathbf{E}\, \mathbf{a}_0 \cdot \mathbf{b}_0$, for $a, b \in \{f, s, n\}$, are the entries of the Green–Lagrange strain tensor $\mathbf{E} = \frac{1}{2} (\mathbf{C} - \mathbf{I})$ in the $(\mathbf{f}_0, \mathbf{s}_0, \mathbf{n}_0)$ frame of reference and B is the bulk modulus. On the other hand, the active stress tensor is defined as:

$$\mathbf{P}^{\mathrm{act}} = T_a \frac{\mathbf{F}\mathbf{f}_0 \otimes \mathbf{f}_0}{\sqrt{\mathcal{I}_{4,f}}}.$$

To model the effect of pericardium on the cardiac wall, we set generalized Robin boundary conditions at the epicardium Γ_0^{epi} (see [89,96]). The boundary condition at the base, accounting for the effect of the neglected part of the domain on the artificial boundary Γ_0^{base}, is derived in Appendix C. Finally, the action of the fluid at the endocardium (Γ_0^{endo}) is modeled by the pressure $p(t)$ (see below).

6.1.4. Blood external circulation

To close the problem, the LV activity must be coupled with the external circulation. With this aim, we consider a lumped description, as done in [89], consisting of four phases, where we conventionally start with systole:

1. In the isovolumetric contraction phase, the pressure $p(t)$ starts from its end-diastolic value ($\bar{p}_{\mathrm{ED}}$) and then raises in such a way that the ventricular volume V is kept constant.
2. When $p(t)$ reaches the aortic valve opening pressure value $\bar{p}_{\mathrm{AVO}}$ (we define such time instant as $t = T^{\mathrm{AVO}}$), the ejection phase starts. In this phase, the evolution of $p(t)$ is modeled by a two-elements Windkessel model [97] as:

   $$\begin{cases} C_{\mathrm{circ}} \dfrac{dp}{dt} = -\dfrac{p}{R_{\mathrm{circ}}} - \dfrac{dV}{dt} & t \in (T^{\mathrm{AVO}}, T^{\mathrm{AVC}}] \\ p(T^{\mathrm{AVO}}) = \bar{p}_{\mathrm{AVO}} \end{cases} \tag{15}$$

   where T^{AVC} (aortic valve closing time) is the first time, after T^{AVO}, when the negative flux $\frac{dV}{dt}$ changes sign.
3. At this stage, another isovolumetric phase begins. This phase ends when $p(t)$ reaches $\bar{p}_{\mathrm{MVO}}$, the value of the mitral valve opening pressure.
4. In the filling phase, we linearly increase $p(t)$ so that it reaches $\bar{p}_{\mathrm{ED}}$ at final time T.

To compute the ventricular volume V we employ the following formula, that is derived in Appendix B:

$$V(t) = \frac{1}{3} \int_{\Gamma_0^{\text{endo}}} J(t)\,(\mathbf{X} + \mathbf{d}(t) - \mathbf{b}(t)) \cdot \mathbf{F}^{-T}(t)\mathbf{N}\, d\Gamma_0,$$

where

$$\mathbf{b}(t) = \frac{1}{\left|\Gamma_0^{\text{base}}\right|} \int_{\Gamma_0^{\text{base}}} (\mathbf{X} + \mathbf{d}(t)) d\Gamma_0.$$

6.1.5. The coupled EM problem

We report here for completeness the coupled EM problem:

$$\begin{cases}
\chi_m \left(C_m \dfrac{\partial v}{\partial t} + \mathcal{I}^{\text{ion}}(v, \mathbf{w}) \right) = \nabla \cdot \left(J\, \mathbf{F}^{-1} \mathbf{D}_m \mathbf{F}^{-T} \nabla v \right) + \mathcal{I}^{\text{app}} & \text{in } \Omega_0 \times (0, T] \\
\dfrac{\partial \mathbf{w}}{\partial t} = \mathbf{h}(v, \mathbf{w}) & \text{in } \Omega_0 \times (0, T] \\
\left(J\, \mathbf{F}^{-1} \mathbf{D}_m \mathbf{F}^{-T} \nabla v \right) \cdot \mathbf{N} = 0 & \text{on } \partial\Omega_0 \times (0, T] \\
v = v_0, \quad \mathbf{w} = \mathbf{w}_0 & \text{in } \Omega_0 \times \{0\} \\
\left(SL - SL_0 \sqrt{\mathcal{I}_{4,f}} \right) - \delta_{SL}^2 \Delta SL = 0 & \text{in } \Omega_0 \times (0, T] \\
\delta_{SL}^2 \nabla SL \cdot \mathbf{N} = 0 & \text{on } \partial\Omega_0 \times (0, T] \\
\dfrac{\partial \mathbf{Z}}{\partial t} = \mathbf{F}(\mathbf{Z}, ([\text{Ca}^{2+}]_{\text{i}}, SL)^T) & \text{in } \Omega_0 \times (0, T] \\
\mathbf{Z}(0) = \mathbf{Z}_0 & \text{in } \Omega_0 \times \{0\} \\
\rho \dfrac{\partial^2 \mathbf{d}}{\partial t^2} - \nabla \cdot \left(\mathbf{P}^{\text{pass}}(\mathbf{d}) + \overline{T}\, G(\mathbf{Z}) \dfrac{\mathbf{F}\mathbf{f}_0 \otimes \mathbf{f}_0}{\sqrt{\mathcal{I}_{4,f}}} \right) = \mathbf{0} & \text{in } \Omega_0 \times (0, T] \\
\mathbf{P}(\mathbf{d})\mathbf{N} + (\mathbf{N} \otimes \mathbf{N}) \left(K_\perp^{\text{epi}} \mathbf{d} + C_\perp^{\text{epi}} \dfrac{\partial \mathbf{d}}{\partial t} \right) & \\
\qquad + (\mathbf{I} - \mathbf{N} \otimes \mathbf{N}) \left(K_\parallel^{\text{epi}} \mathbf{d} + C_\parallel^{\text{epi}} \dfrac{\partial \mathbf{d}}{\partial t} \right) = \mathbf{0} & \text{on } \Gamma_0^{\text{epi}} \times (0, T] \\
\mathbf{P}(\mathbf{d})\mathbf{N} = \dfrac{\| J\mathbf{F}^{-T}\mathbf{N} \|}{\int_{\Gamma_0^{\text{base}}} \| J\mathbf{F}^{-T}\mathbf{N} \| d\Gamma_0} \displaystyle\int_{\Gamma_0^{\text{endo}}} p J\mathbf{F}^{-T}\mathbf{N} d\Gamma_0 & \text{on } \Gamma_0^{\text{base}} \times (0, T] \\
\mathbf{P}(\mathbf{d})\mathbf{N} = -p J\mathbf{F}^{-T}\mathbf{N} & \text{on } \Gamma_0^{\text{endo}} \times (0, T] \\
\mathbf{d} = \mathbf{d}_0, \quad \dfrac{\partial \mathbf{d}}{\partial t} = \dot{\mathbf{d}}_0 & \text{in } \Omega_0 \times \{0\},
\end{cases} \tag{16}$$

where the endocardial pressure p has to be determined, depending on the cardiac cycle phase, either as Lagrange multiplier for the isovolumetric phases, or as solution of the circulation model (15). In Table 2 we report the full list of parameters used in the EM model.

6.2. Numerical discretization

For the spatial discretization of the first equation of Eq. (10), for Eqs. (11)–(13) and for the generation of fibers fields, we employ $P1$ linear Finite Elements on a tetrahedral mesh. Moreover, we discretize the ionic variables $\mathbf{w}$ and the activation variables $\mathbf{Z}$ by means of $P1$ linear Finite Elements, and we solve the associated ODE models (i.e. the equation for $\mathbf{w}$ of Eqs. (10) and (12)) at each nodal point of the computational mesh. As for the time discretization, we consider a uniform subdivision $0 = t_0 < t_1 < \cdots < t_M = T$ of the time interval $[0, T]$ with step $\Delta t = 2 \times 10^{-4}$ s. To denote the unknown at the kth time step, we use a superscript (e.g. $v^{(k)} \approx v(t_k)$). For the discretization of time derivatives, we use first order finite difference schemes [81].

Table 2
Parameters of the EM problem.

Variable	Value	Unit	Description
Electrophysiology			
σ_f	1.204×10^3	$\mathrm{mm}^2\,\mathrm{s}^{-1}$	Normalized electrical diffusivity in fiber direction
σ_{iso}	0.1761×10^3	$\mathrm{mm}^2\,\mathrm{s}^{-1}$	Normalized electrical diffusivity in transverse direction
$\mathcal{I}^{\max}$	100	$\mathrm{V\,s}^{-1}$	Applied current value
δ	14	mm	Applied current radius
t_{app}	2×10^{-3}	s	Applied current duration
Activation			
$\overline{T}$	700	kPa	Active tension per unit area if $y = 1$
SL_0	2.0	µm	Reference sarcomere length
δ_{SL}	5	mm	SL regularization radius
Mechanics			
ρ	1×10^3	$\mathrm{kg\,m}^{-3}$	Tissue density
B	50	kPa	Bulk modulus
C	2	kPa	Material stiffness
b_{ff}	8	–	Hyperelastic parameter
b_{ss}	6	–	Hyperelastic parameter
b_{nn}	3	–	Hyperelastic parameter
b_{fs}	12	–	Hyperelastic parameter
b_{fn}	3	–	Hyperelastic parameter
b_{sn}	3	–	Hyperelastic parameter
$K_{\perp}^{\mathrm{epi}}$	2×10^{-1}	$\mathrm{kPa\,mm}^{-1}$	Robin boundary condition
$C_{\perp}^{\mathrm{epi}}$	2×10^{-2}	$\mathrm{kPa\,s\,mm}^{-1}$	Robin boundary condition
$K_{\parallel}^{\mathrm{epi}}$	2×10^{-2}	$\mathrm{kPa\,mm}^{-1}$	Robin boundary condition
$C_{\parallel}^{\mathrm{epi}}$	2×10^{-3}	$\mathrm{kPa\,s\,mm}^{-1}$	Robin boundary condition
Circulation			
R_{circ}	3.5×10^{-2}	$\mathrm{Pa\,s\,mm}^{-3}$	Windkessel model parameters
C_{circ}	4.5	$\mathrm{mm}^3\,\mathrm{Pa}^{-1}$	Windkessel model parameters
$\bar{p}_{\mathrm{ED}}$	1.333	kPa	End-diastolic pressure
$\bar{p}_{\mathrm{AVO}}$	9.333	kPa	Aortic valve opening pressure
$\bar{p}_{\mathrm{MVO}}$	0.667	kPa	Mitral valve opening pressure

To couple the different models, we employ the segregated strategy presented in [98]. Specifically, at each time step t_k, we orderly perform the following steps:

I. We update the ionic variables of the ten Tusscher–Panfilov model [92], with an IMEX scheme, to deal with the stiff nature of the equations.
II. We update the potential field $v^{(k)}$ by solving the monodomain equation (Eq. (10)), with implicit treatment of the potential and by employing an extrapolation of the displacement $\mathbf{d}$ consistent with the order of the time derivative discretization.
III. We recover the local sarcomere length by solving Eq. (11) and we update the activation variables by solving Eq. (12), with explicit treatment of the unknown $\mathbf{Z}$. Since the solution of the activation model requires a smaller time step (2.5×10^{-5} s), at this step we perform an inner iteration.
IV. We update the displacement by Eq. (13), with implicit treatment of the unknown $\mathbf{d}^{(k)}$. To deal with the nonlocal nature of the boundary condition on Γ_0^{base}, we adopt a quasi-Newton strategy, by computing the Jacobian matrix only with respect to the local terms. In the isovolumetric phases of the heartbeat, we solve Eq. (13) together with the equation $V^{(k)} = V^{(k-1)}$. This is a saddle-point problem in the unknowns $\mathbf{d}^{(k)}$ and $p^{(k)}$ and we solve it by Schur complement reduction [99]. On the other hand, during the ejection phase, the pressure is updated before solving the mechanical problem with an implicit treatment of p. In Test Case 3, to lower the computational burden due to the fine mesh, for the solution of the mechanical problem we employ a 5 times larger time step (see [98,100]).

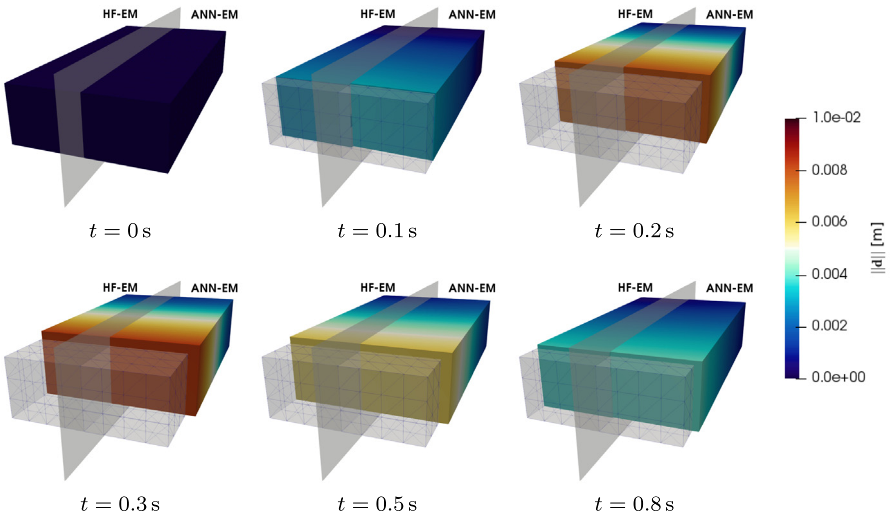

Fig. 3. Test Case 1: comparison of the displacement field (at different time steps) between the simulations performed by the HF activation model and by the ANN model. For visualization purposes, the domain is split into two identical subregions: in the left subregion, the solution obtained with the HF activation model is shown; in the right subregion, the solution obtained with the ANN-based activation model.

6.3. *ANN-based efficient EM simulations*

The computational cost associated with the numerical approximation of the EM problem is strongly affected by the solution of the 2176-variables activation model (12), both in terms of memory storage and computational time (we provide quantitative indications in Sections 6.4–6.5). To lower such computational burden, we replace the HF activation model (12) with its surrogate given by the 2-variables ANN model (3). This can be easily done thanks to the fact that the two models share the same inputs and outputs. In the following, we compare the results of EM simulations obtained by employing the HF activation model and by employing the ANN model, which we will respectively denote by HF-EM and ANN-EM.

6.4. *Test Case 1: cardiac slab*

We consider a slab of cardiac tissue, defined by the computational domain $\Omega_0 = (0, 40\text{ mm}) \times (0, 20\text{ mm}) \times (0, 8\text{ mm})$. We consider a fiber field $\mathbf{f}_0 = \mathbf{e}_1$ aligned as the x-axis and a sheet field $\mathbf{s}_0 = \mathbf{e}_3$ aligned as the z-axis. We consider a unique stimulus location $\mathbf{x}_1 = (0, 0, 0)^T$ (point A of Fig. 4). Due to the simple domain employed, in this test case the three boundaries (Γ_0^{base}, Γ_0^{epi} and Γ_0^{endo}) are not defined. Thus, we change the boundary conditions of the mechanical problem (13), by imposing $\mathbf{d} \cdot \mathbf{N} = 0$ and a no-stress condition in tangential direction on the three faces passing through the origin (i.e. $\{\mathbf{x} \colon \mathbf{x} \cdot \mathbf{e}_j = 0\}$, for $j = 1, 2, 3$). In the remaining subset of the boundary, we impose a generalized boundary condition with $K_\perp = 5 \times 10^{-1}$ kPa mm, $C_\perp = 1 \times 10^{-1}$ kPa mm and $K_\parallel = C_\parallel = 0$.

We consider a structured computational mesh with a uniform subdivision in 16, 8 and 3 elements along the cartesian directions x, y, and z, respectively, for a total of 2304 tetrahedra and 612 dofs. In Figs. 3–4 we show a comparison between the HF-EM and the ANN-EM results. The computational costs are compared in Table 4.

6.5. *Test Cases 2 and 3: idealized and patient-specific left ventricle*

We consider an idealized LV (Test Case 2) and a realistic LV derived from the Zygote CAD [101] (Test case 3). The idealized computational mesh consists of 6500 tetrahedra and 1827 degrees of freedom (see Fig. 5a), whereas the patient-specific one accounts for $354 \cdot 10^3$ tetrahedra and $65 \cdot 10^3$ degrees of freedom (see Fig. 5b). The electrical stimulus $\mathcal{I}^{\text{app}}$ is applied at three points, located on the endocardial surface close to the apex. We generate the fibers and sheets distribution according to the rule-based algorithm proposed in [102], by setting $\alpha_{\text{endo}} = -60°$,

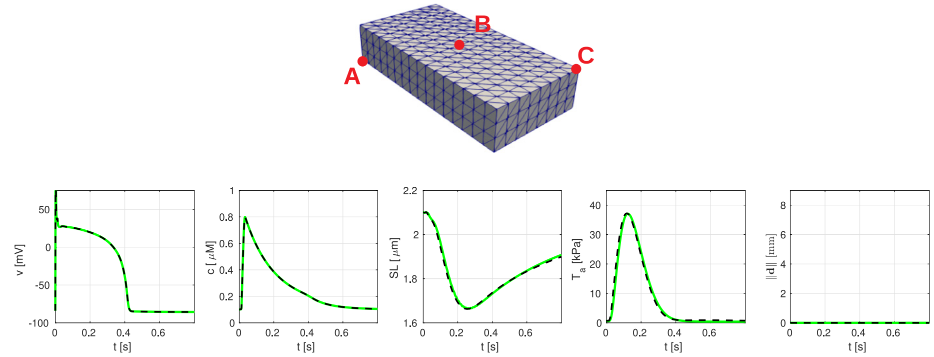

(a) Point A

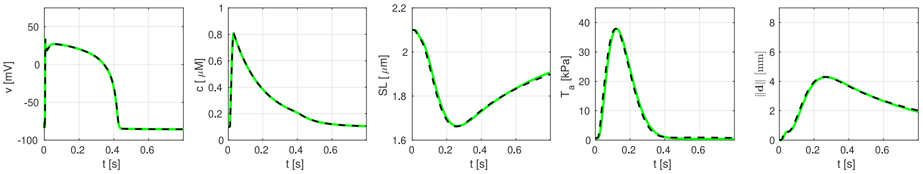

(b) Point B

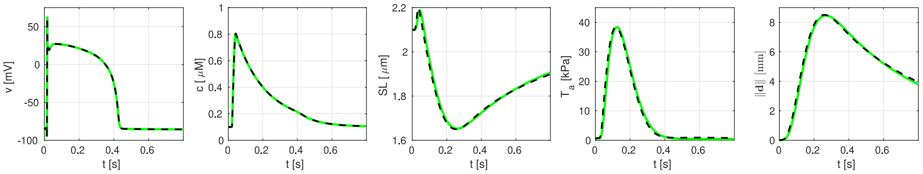

(c) Point C

Fig. 4. Test Case 1: comparison of the time course of quantities of interest in three points (indicated in the top image) obtained with the simulations performed with HF-EM (solid colored lines) and with ANN-EM (black dashed lines).

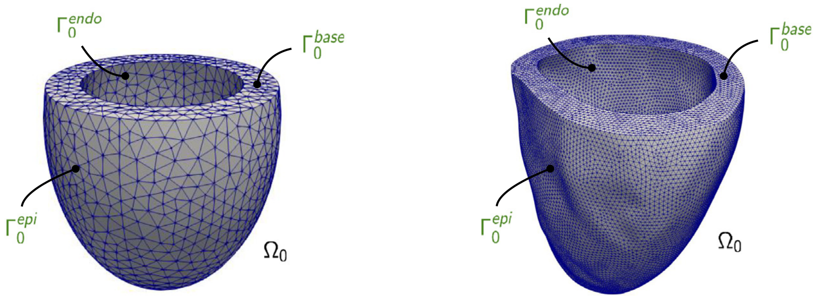

(a) Test case 2 (b) Test case 3

Fig. 5. LV computational meshes of Test Case 2 and 3.

$\alpha_{\text{epi}} = +60°$. The fibers, sheets and normal fields are displayed (just for the patient-specific geometry) in Fig. 6. In Test Case 2 we set the parameter $\overline{T}$ to 480 kPa, to obtain realistic pressure values.

The stress–strain relationship defined by (14) is referred to the natural configuration. However, in practical applications, the natural stress-free configuration is unknown since an internal pressure p is always present in each phase of the heartbeat. In Test Case 2, we assume that the computational domain is referred to the end dyastolic phase. Therefore, we recover the natural configuration as the domain such that by applying the pressure $p = \bar{p}_{\text{ED}}$, one recovers the given computational domain as steady-state solution. Then, we employ such deformation as initial

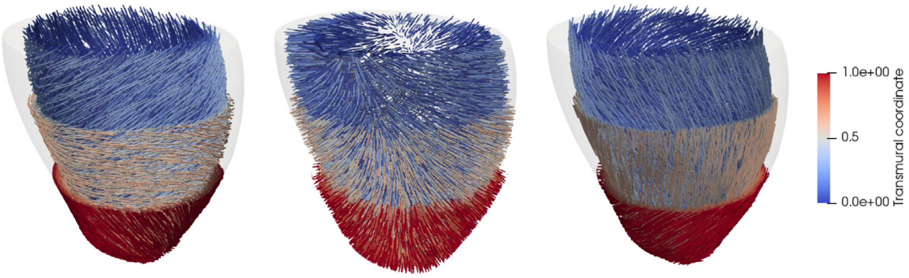

(a) Field $\mathbf{f}_0$ (b) Field $\mathbf{s}_0$ (c) Field $\mathbf{n}_0$

Fig. 6. Test Case 3: representation of fibers, sheets and normal fields. Three sections in the apico-basal direction allow to appreciate the transmural variation of fibers orientation.

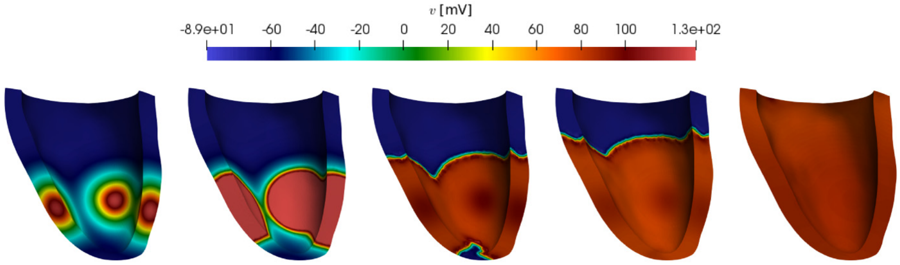

$t = 1\,\text{ms}$ $t = 2\,\text{ms}$ $t = 6\,\text{ms}$ $t = 15\,\text{ms}$ $t = 35\,\text{ms}$

Fig. 7. Test Case 3: transmembrane potential at different times.

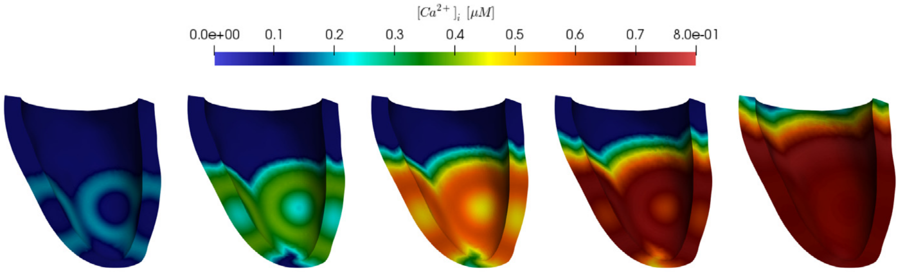

$t = 10\,\text{ms}$ $t = 15\,\text{ms}$ $t = 20\,\text{ms}$ $t = 25\,\text{ms}$ $t = 40\,\text{ms}$

Fig. 8. Test Case 3: intracellular calcium concentration at different times.

condition for the mechanical problem (13). On the other hand, as the computational domain of Test Case 3 is associated to a phase of the heart cycle such that the diastolic filling is not fully completed (more precisely, the beginning of the atrial kick), we recover the natural configuration by assuming that the computational domain is at equilibrium with an intermediate pressure between $\bar{p}_{\text{ED}}$ and the pressure at the end of the second isovolumetric phase (specifically we take $p = 5.6$ mmHg). Then, we passively inflate the ventricle until we reach the pressure $\bar{p}_{\text{ED}}$, and we employ the obtained displacement as initial condition for the mechanics problem (13).

In Figs. 7 and 8 we show the propagation of the v and the c fields, respectively, for Test Case 3. The active tension field T_a is visualized, at different time steps, in Fig. 9, where three sections at different quotes along the apex-base coordinate allow to appreciate the distribution of active stress across the transmural coordinate. In Fig. 9 we also report the spatial distribution of the relative error between the active tension fields obtained with the HF-EM and the ANN-EM paradigms. The results are commented in Section 7. Finally, in Fig. 10 (Test case 2) and in Fig. 11 (Test case 3), we show the displacement field and the contraction of the LV. The top and frontal sections highlight the torsion that the LV undergoes during the heartbeat and the wall thickening.

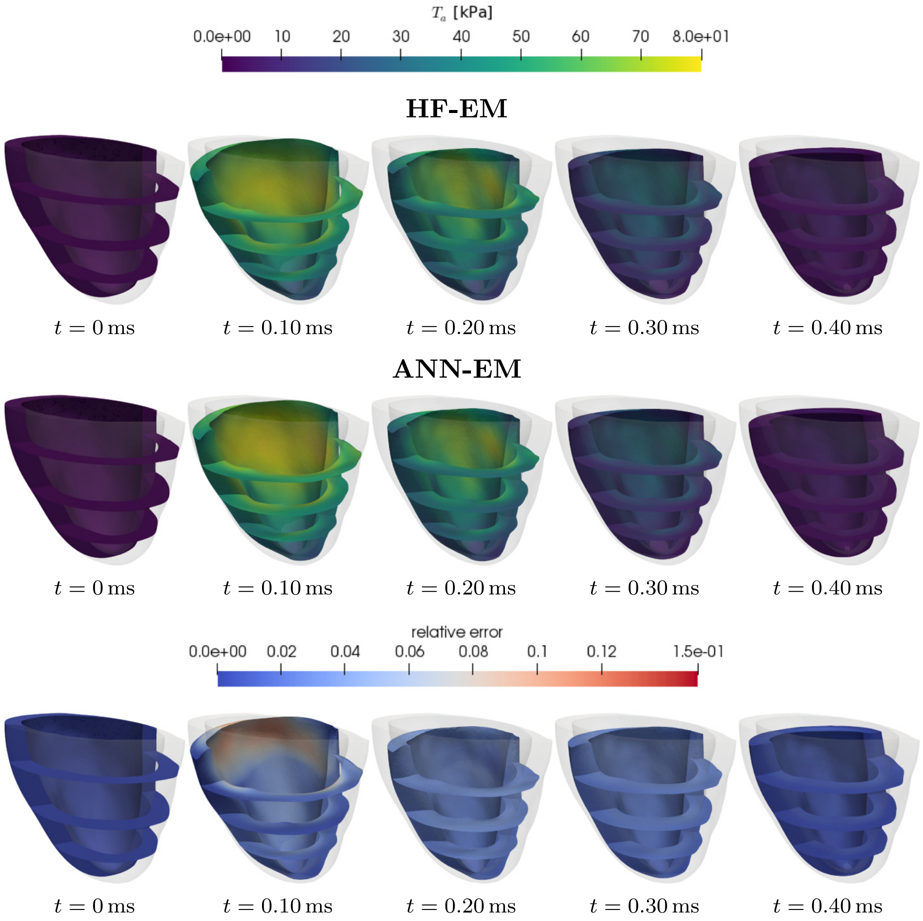
T_a [kPa]
0.0e+00
10
20
30
40
50
60
70
8.0e+01
HF-EM
$t = 0\,\mathrm{ms}$
$t = 0.10\,\mathrm{ms}$
$t = 0.20\,\mathrm{ms}$
$t = 0.30\,\mathrm{ms}$
$t = 0.40\,\mathrm{ms}$
ANN-EM
$t = 0\,\mathrm{ms}$
$t = 0.10\,\mathrm{ms}$
$t = 0.20\,\mathrm{ms}$
$t = 0.30\,\mathrm{ms}$
$t = 0.40\,\mathrm{ms}$
relative error
0.0e+00
0.02
0.04
0.06
0.08
0.1
0.12
1.5e-01
$t = 0\,\mathrm{ms}$
$t = 0.10\,\mathrm{ms}$
$t = 0.20\,\mathrm{ms}$
$t = 0.30\,\mathrm{ms}$
$t = 0.40\,\mathrm{ms}$

Fig. 9. Test Case 3: active tension at different times obtained with HF-EM (first row) and ANN-EM (second row) and the corresponding relative error (third row).

Table 3
Test Cases 2 and 3: main cardiac indicators. Comparison between the HF-EM and the ANN-EM frameworks and corresponding relative errors.

Indicator	HF-EM	ANN-EM	Relative error
Test Case 2 (idealized LV, 1827 dof)			
Stroke volume (mL)	63.33	63.57	3.71×10^{-3}
Ejection fraction (%)	46.63	46.80	3.71×10^{-3}
Maximum pressure (mmHg)	112.96	113.91	8.38×10^{-3}
Work (mJ)	766	773	9.08×10^{-3}
Test Case 3 (patient-specific LV, 65476 dof)			
Stroke volume (mL)	56.64	56.39	4.33×10^{-3}
Ejection fraction (%)	44.48	44.29	4.33×10^{-3}
Maximum pressure (mmHg)	108.94	109.10	1.52×10^{-3}
Work (mJ)	662	659	4.85×10^{-3}

Then, in Fig. 12 (Test case 2) and Fig. 13 (Test case 3), we compare the results obtained within the HF-EM and the ANN-EM paradigms. In the top row, we show the time evolution, of the average, minimum and maximum values over the domain of $[\mathrm{Ca}^{2+}]_\mathrm{i}$, SL and T_a. In the bottom row we show the time evolution of the macroscopic quantities p and V and the LV pressure–volume loop. All the curves show a good match between the results obtained in the HF-EM and the ANN-EM paradigms.

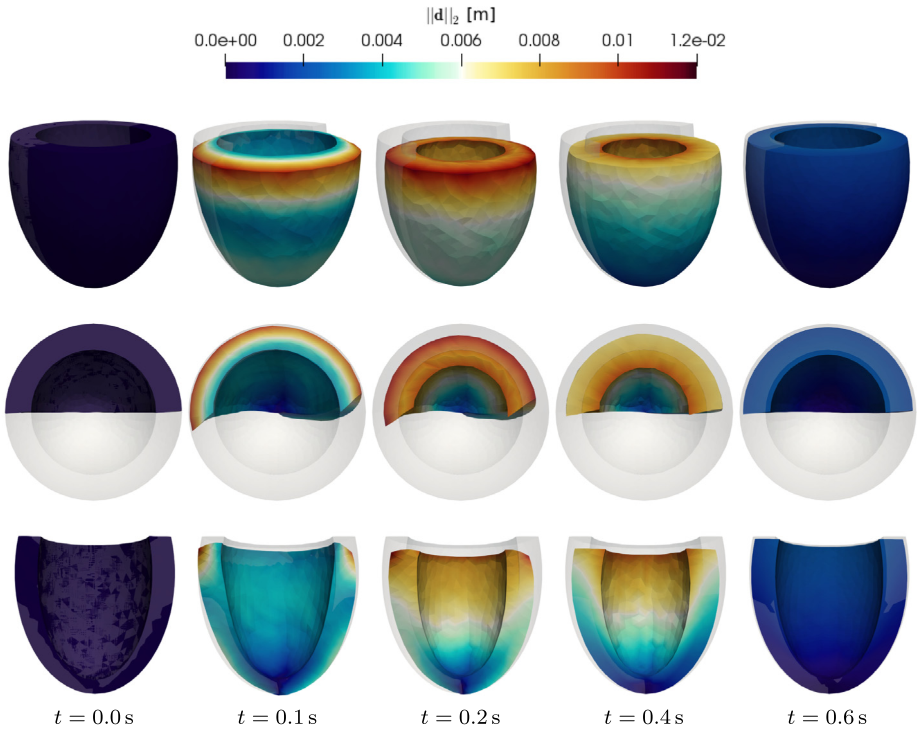

Fig. 10. Test Case 2: deformed geometry and magnitude of displacement at different times. Top row: full geometry. Middle row: half domain (top view). Bottom row: half domain (frontal view).

Table 4
Comparison of the computational times associated to the four physics and the total wall time between HF-EM and ANN-EM, for both test cases.

Simulation type	Ionic	Potential	Activation	Mechanics	Wall time
Test Case 1 (cardiac slab, 612 dof, 1 core)					
HF-EM	6.3%	0.3%	89.0%	4.5%	3 h 16′
ANN-EM	53.0%	2.7%	3.3%	41.1%	22′
Test Case 2 (idealized LV, 1827 dof, 1 core)					
HF-EM	4.27%	0.29%	91.94%	3.40%	9 h 31′
ANN-EM	53.38%	3.31%	3.74%	39.57%	46′
Test Case 3 (patient-specific LV, 65476 dof, 20 cores)					
HF-EM	3.14%	0.47%	83.07%	13.33%	20 h 18′
ANN-EM	41.21%	4.80%	2.54%	51.46%	2 h 04′

The main cardiac biomarkers, some of them clinically meaningful, computed in the HF-EM and ANN-EM paradigms, are reported in Table 3. For all the biomarkers, the error between HF-EM and ANN-EM is even smaller than the train and the test error associated with the ANN model. We will comment on this in Section 7.

Finally, in Table 4, we report the computational times associated with the numerical approximation of the EM problem in the HF-EM and in the ANN-EM paradigms. For Test Case 2, a single core was employed, whereas for Test Case 3 simulations were run in parallel on 20 cores.

7. Discussion

7.1. Computational gain

The ANN-EM paradigm accomplishes a significant reduction of the computational cost of the HF-EM paradigm. The solution of the activation model, which accounts for most of the computational time of the whole simulation,

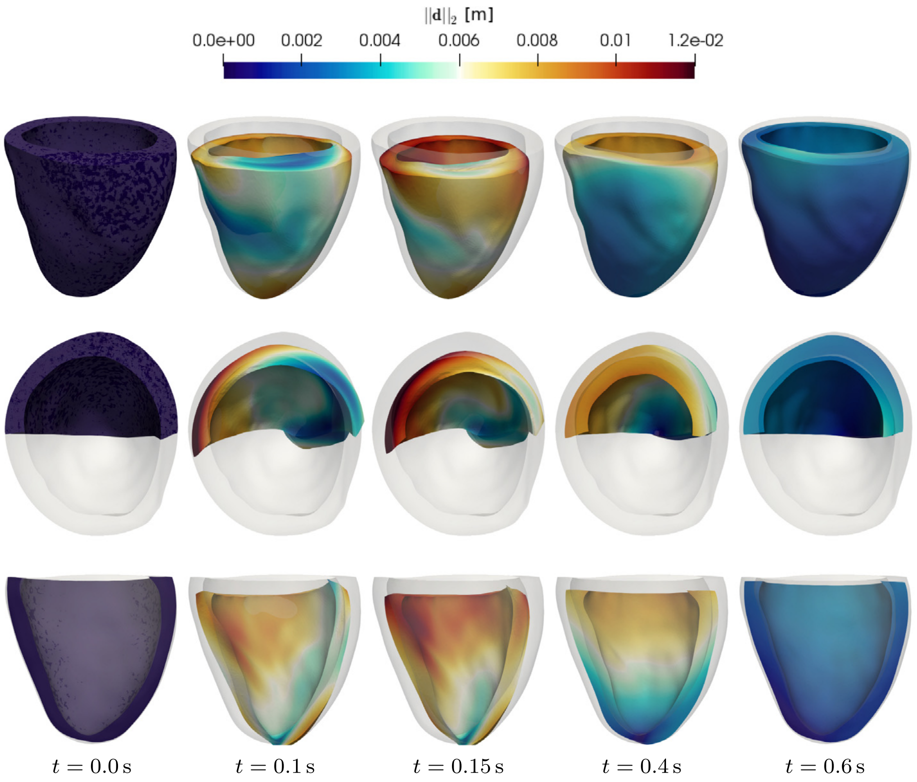

Fig. 11. Test Case 3: deformed geometry and magnitude of displacement at different times. Top row: full geometry. Middle row: half domain (top view). Bottom row: half domain (frontal view).

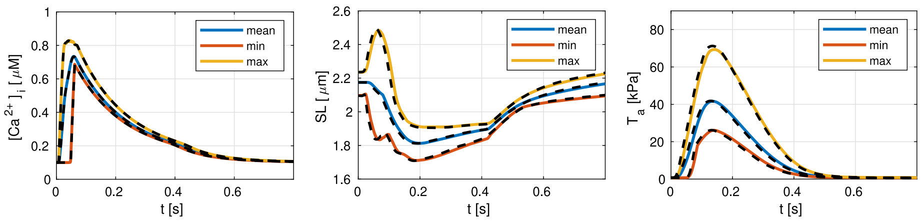

(a) Calcium concentration (b) Sarcomere length (c) Active tension

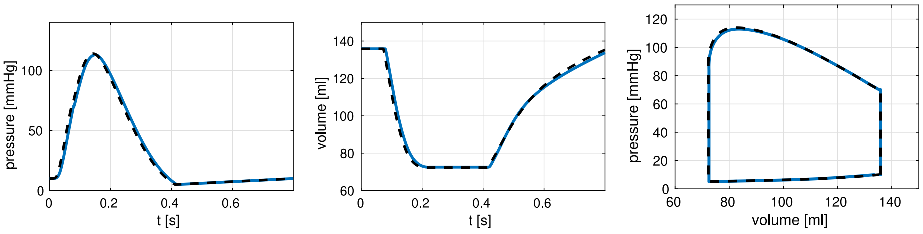

(d) Endocardial pressure (e) LV volume (f) Pressure-volume loop

Fig. 12. Test Case 2: comparison of the time evolution of quantities of interest and of the pressure–volume loop obtained with the simulations performed with HF-EM (solid colored lines) and with ANN-EM (black dashed lines). In (a)–(b)–(c) the three lines show the time evolution of the minimum, maximum and mean values of $[\mathrm{Ca}^{2+}]_\mathrm{i}$, SL and T_a over the computational domain.

highlights a gain nearly of a factor 300 in all test cases, reducing the overall computational times by one order of magnitude. The computational speedup is slightly smaller for finer grids, for which the relative weight of

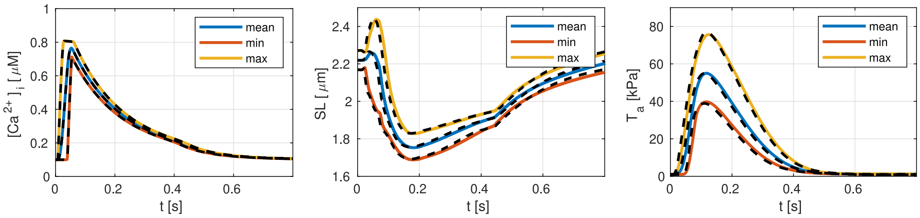

(a) Calcium concentration (b) Sarcomere length (c) Active tension

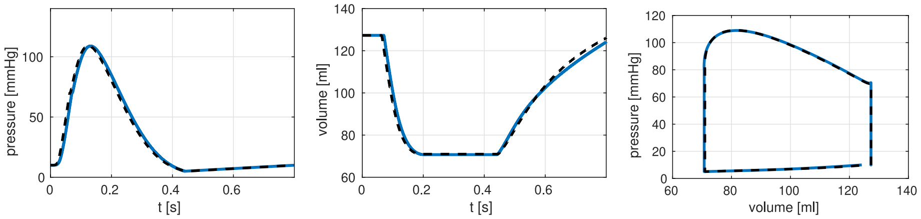

(d) Endocardial pressure (e) LV volume (f) Pressure-volume loop

Fig. 13. Test Case 3: comparison of the time evolution of quantities of interest obtained in the HF-EM and the ANN-EM frameworks (see caption of Fig. 12).

the mechanical subproblem is more pronounced. However, whereas the approximation of the electrophysiology subproblem (10) requires a finer grid for the convergence of the solution [6], the computational mesh used in Test Case 3 features a large enough number of elements to get accurate results for the mechanics subproblem (13) and to capture the complexity of patient-specific domains [6,38]. Therefore, since when different meshes are employed for the different physics the activation subproblem (12) is typically solved on the mesh used for the mechanics [6], we expect that the speedup obtained in Test Case 3 is representative for the computational gain one can obtain for HF simulations of patient-specific EM.

With the ANN-EM approach, the number of variables for each degree of freedom of the domain is 24 (18 ionic variables, the transmembrane potential, 2 activation variables, 3 components of the displacement), significantly lower than the number of variables with the HF-EM approach ($18 + 1 + 2176 + 3 = 2198$).

Finally, we remark that in this work we considered a staggered approach [98,100], where the four different physics are solved in sequence. The results could vary with other numerical coupling approaches. In particular, with a monolithic approach (where the 4 physics are solved simultaneously in a strongly coupled manner [89]), the computational gain is expected to be even greater since the size of the Jacobian matrix scales as the square of the number of variables.

7.2. Approximation accuracy

The zero-dimensional simulations obtained with the reduced ANN model (see Section 5.2) are accurate with respect to the ones obtained with the HF model (relative error of order 10^{-2}). Nevertheless, when the activation model is embedded in the EM coupled system, the model output (i.e. active force) has a feedback not only on its inputs (mostly on SL, as it causes the tissue contraction, but also on $[\mathrm{Ca}^{2+}]_\mathrm{i}$, due to the mechano-electrical feedback). Therefore, one should check whether such feedback has the effect of amplifying the error introduced by the ANN reduced model, or not.

Numerical results show that the errors are kept under control when the ANN model is embedded in a EM setting. The largest error between the active tension obtained with the ANN-EM and the HF-EM paradigms is attained at the time of maximum activation (i.e. $t = 0.1$ s), as shown in Fig. 9. A deeper analysis reveals that the discrepancy between the two results is related to a small anticipation (nearly 5×10^{-3} s) in the activation dynamics obtained in the ANN-EM paradigm with respect to that obtained with the HF-EM one. We believe that this is due to the time-discretization error associated to the training phase, during which a larger time-step ($\Delta t = 1 \times 10^{-2}$ s) than the one used for the EM simulation ($\Delta t = 2 \times 10^{-4}$ s) is employed. We plan to investigate this aspect in future works. Nonetheless, the small anticipation of the active stress peak does not compromise the quality of the results. As a matter of fact, the errors associated to the main cardiac biomarkers (order of 10^{-3}) are dampened by one order of magnitude with respect to the errors obtained with zero-dimensional simulations of the activation model alone. Indeed, the feedback of mechanics on activation has a favorable effect: a positive deviation of active tension leads to a larger shortening of the tissue (i.e. lower SL), which, in turn, makes the active tension decrease, compensating the initial error in T_a. This is a consequence of the fact that the heart works on the ascending limb of the force–length relationship (on the descending limb, which occurs when the tissue is over-stretched, we would have the opposite effect). It is indeed recognized [15,16] that the advantage of this fact lies in an enhanced stability in the contraction of the heart. In Appendix D we prove, in a simplified one-dimensional setting, that the error in the ANN-EM setting (with respect to HF-EM) is lower than the error of the ANN model alone (with respect to the HF model).

7.3. Comparison with phenomenological models

The ANN model is built from data generated by the HF model. This is somehow similar to the way the so-called phenomenological models, i.e. models built by fitting the experimental observations with a few number of variables (see e.g. [32–34,36]), are built. A natural question is how those models compare with the ANN model.

Building a model consists in the solution of an inverse problem: starting from experimental observations, one looks for a law, written in mathematical terms, and a set of parameters describing the phenomenon that generated the observations themselves. However, experimental data are typically noisy and defective. This is particularly evident in the case considered in this work, due to the microscopic scale at which force is generated and to the intrinsic difficulties in performing experimental measurements of the internal properties of myofilaments without damaging them [25,26,28]. In the context of inverse problems and statistical learning, the action of compensating for noise and deficiency of data is known as *regularization* (see e.g. [103,104]). Regularization is typically performed either by suitable penalization of the unknown variables, or by restricting the set of candidate solutions [105].

Phenomenological models are derived by finding the best fit of experimental data with a simple law chosen a priori. Such a priori assumptions allow for a lumped description of the phenomenon with a small number of parameters to be tuned from experimental data. This is crucial, due to the noisy and defective nature of data. In fact, such a priori assumptions are a way of performing regularization. For instance, to reproduce the nonlinear response of activation to calcium concentration – consequence of the nearest-neighborhood interaction within units – without explicitly representing the units themselves, a power law dependence on $[\mathrm{Ca}^{2+}]_\mathrm{i}$ is typically assumed, and the exponent is estimated by fitting experimental data. However, this law has a phenomenological basis and it is not derived by first principles [34].

With our approach, instead, regularization is performed during the construction of the HF model thanks to the introduction of physics first principles and to a detailed description of the microscopic arrangement of the contractile system. In such a way, indeed, the set of possible relationships among the variables is restricted to those satisfying some physical principles. However, a detailed physics-based description leads to complex models (in the previous example, a biophysically-detailed description of nearest-neighborhood interactions within units is not possible without a spatially-explicit description of the filament). On the other hand, establishing a model on physics principles clearly enhances its predictive power. Then, in a second stage, the ROM is learned from the HF model, which does not suffer from the problems affecting experimental data: training data can be generated from the HF model without noise and without constraints on the quantity. This allows to fit data within a much wider class of candidate solutions (specifically, we fit training data with ANN-based models, which are able to virtually represent all ODE models, if a sufficient number of neurons is used, as proved in [13]).

To summarize, whereas phenomenological models are directly derived from experimental observations, with our approach the process is split into two stages. First, we build an HF model, by compensating for the deficiency and bad quality of experimental data thanks to physics. Then, in a second stage, we build a ROM, by fitting data (no more noisy or defective) generated by HF model. Thus, the ROM should be seen merely as a way of efficiently solving the physics-based model itself.

A further advantage of building a model on the ground of a microscopical description is this allows to investigate the effects of microscopical properties on the macro-level tissue features (e.g. study the effect of drugs affecting the binding rate of myofilament proteins), whereas the parameters of phenomenological models may not have a clear physical interpretation.

8. Conclusions

We proposed a novel strategy to reduce the computational burden of cardiac multiscale EM simulations, wherein the intrinsically complex subcellular mechanisms leading to the activation of the muscular tissue make it difficult to trade off the detail of description of activation models (and thus their reliability) with computational efficiency. Specifically, we built an ANN-based ROM of a complex and detailed model of cardiac activation, featuring more that 2000 variables. This operation, thanks to the scale separation between the organ and the myofilaments, can be performed offline, without any dependence on the three-dimensional setting where we later embed the ROM. The ANN learns, within a gray-box approach, the dynamics of the HF model from a collection of input–output pairs, generated by the HF model itself, combined with some a priori knowledge, enforced during the learning process. In such a way we have derived a 2-variables ROM, capable of reproducing the results of the HF model with a relative error of about 10^{-2}. Moreover, we have validated the results of the ANN-based model, by checking that it is still able to reproduce the experimental characterizations that the HF model can reproduce.

By employing the ANN-based ROM in the context of multiscale EM, the computational time associated to the solution of the activation subproblem is reduced by nearly 300 times, leading – in the case of the computational grids employed in this work – to a one order of magnitude decrease of the overall computational time required to approximate the EM problem. Moreover, the number of variables for each degree of freedom reduces from 2198 to just 24, a significant gain, especially when large-scale simulations are addressed. Remarkably, thanks to the stabilizing effect of the SL feedback on the activation dynamics, the relative error in the main cardiac biomarkers introduced by employing the ANN-based ROM in the context of EM is just of about 10^{-3}. We conclude that, in virtue of the offline ANN learning of the complex activation subproblem, a very favorable balance between reliability and computational efficiency is achieved, without any compromise on the details of description of the microscopic phenomena pertaining to the generation of force.

Declaration of competing interest

The authors declare the following financial interests/personal relationships which may be considered as potential competing interests: The authors are preparing a patent application related to some topics partially covered in the manuscript.

Acknowledgments

This project has received funding from the European Research Council (ERC) under the European Union's Horizon 2020 research and innovation programme (Grant Agreement No. 740132, iHEART — An Integrated Heart Model for the simulation of the cardiac function, P.I. Prof. A. Quarteroni). The authors gratefully acknowledge Dr. M. Fedele (MOX, Politecnico di Milano) for having provided the computational mesh of Test Case 3 and Dr. A. Gerbi (EPFL) for the interesting discussions about integrated cardiac modeling.

Appendix A. The ANN-based model

The ANN-based model considered in this paper can be written in the form of (3), where the right hand side is given by the following ANN:

$$\mathbf{f}(\mathbf{z}, \mathbf{u}) = \mathbf{W}_2 \tanh\left(\mathbf{W}_1 \tanh\left(\mathbf{W}_0(\mathbf{z}^T, \mathbf{u}^T)^T - \boldsymbol{\vartheta}_0\right) - \boldsymbol{\vartheta}_1\right) - \boldsymbol{\vartheta}_2.$$

The application of the operator tanh has to be intended componentwise. The value of the weight matrices $\mathbf{W}_j$ and of the bias vectors $\boldsymbol{\vartheta}_j$ (where $j = 0, 1, 2$) are made available in the following online repository, together with MATLAB and PYTHON codes to perform numerical simulations with the ANN model:
https://github.com/FrancescoRegazzoni/cardiac-activation-ann

The training of the ANNs has been carried out with the MATLAB library `model-learning`, which is also available online [106]:
https://github.com/FrancescoRegazzoni/model-learning

Appendix B. Ventricular volume computation

In order to compute the ventricular volume V (i.e. the volume of the ventricular cavity), we proceed as follows. First, we identify the center point of the base as:

$$\mathbf{b}(t) = \frac{1}{\left|\Gamma_0^{\text{base}}\right|} \int_{\Gamma_0^{\text{base}}} (\mathbf{X} + \mathbf{d}(t)) d\Gamma_0,$$

where $\mathbf{X}$ denotes the material coordinate. Then, we close the ventricular cavity by the surface Γ_t^{cap}, defined as the surface connecting the point $\mathbf{b}(t)$ with the orifice ring. The ventricular volume is thus defined as the measure of the volume Ω_t^{fluid}, delimited by Γ_t^{endo} and Γ_t^{cap}. By exploiting the identity $\nabla \cdot (\mathbf{x} - \mathbf{b}(t)) = 3$, where $\mathbf{x}$ denotes the spatial coordinate, we have:

$$\begin{aligned} 3V(t) &= \int_{\Omega_t^{\text{fluid}}} 3\, d\mathbf{x} = \int_{\Omega_t^{\text{fluid}}} \nabla \cdot (\mathbf{x} - \mathbf{b}(t))\, d\mathbf{x} \\ &= \int_{\Gamma_t^{\text{endo}}} (\mathbf{x} - \mathbf{b}(t)) \cdot \mathbf{n}(t)\, d\Gamma + \int_{\Gamma_t^{\text{cap}}} (\mathbf{x} - \mathbf{b}(t)) \cdot \mathbf{n}(t)\, d\Gamma, \end{aligned}$$

where $\mathbf{n}(t)$ and $\mathbf{N}$ denote the outer normal at the surface in the actual and reference domains respectively. Since, by construction, $(\mathbf{x} - \mathbf{b}(t)) \perp \mathbf{n}(t)$ on Γ_t^{cap}, the second term vanishes, leading to the formula:

$$V(t) = \frac{1}{3} \int_{\Gamma_0^{\text{endo}}} J(t)\, (\mathbf{X} + \mathbf{d}(t) - \mathbf{b}(t)) \cdot \mathbf{F}^{-T}(t) \mathbf{N}\, d\Gamma_0,$$

Appendix C. Boundary conditions for the mechanics problem

The base Γ_0^{base} is an artificial boundary and, as such, it must be provided with boundary conditions which account for the effect of the neglected part of the domain on the considered part. We respectively denote by $\widetilde{\Omega}_t$ and $\widetilde{\Omega}_t^{\text{fluid}}$ the solid and fluid domains located above the base, and by $\widetilde{\Gamma}_t^{\text{endo}}$, $\widetilde{\Gamma}_t^{\text{epi}}$ the endocardial end epicardial surfaces located above the base. By considering a quasistatic approximation and by denoting the Cauchy stress tensor by $\mathbf{T} = \mathbf{T}^{\text{pass}} + \mathbf{T}^{\text{act}}$, the momentum equation in the current configuration entails:

$$\mathbf{0} = \int_{\widetilde{\Omega}_t} \nabla \cdot \mathbf{T}\, d\mathbf{x} = \int_{\partial \widetilde{\Omega}_t} \mathbf{T}\mathbf{n}\, d\Gamma_t = \int_{\widetilde{\Gamma}_t^{\text{epi}}} \mathbf{T}\mathbf{n}\, d\Gamma_t + \int_{\widetilde{\Gamma}_t^{\text{endo}}} \mathbf{T}\mathbf{n}\, d\Gamma_t + \int_{\widetilde{\Gamma}_t^{\text{base}}} \mathbf{T}\mathbf{n}\, d\Gamma_t.$$

We assume that the epicardial surface located above the base is unloaded [96], that is $\mathbf{T}\mathbf{n} = \mathbf{0}$ on $\widetilde{\Gamma}_t^{\text{epi}}$. On $\widetilde{\Gamma}_t^{\text{endo}}$, which is in contact with the fluid, we have $\mathbf{T}\mathbf{n} = -p\mathbf{n}$. Moreover, we have the following identity:

$$\mathbf{0} = \int_{\Omega_t^{\text{fluid}} \cup \widetilde{\Omega}_t^{\text{fluid}}} \nabla p\, d\mathbf{x} = \int_{\Gamma_t^{\text{endo}}} p\mathbf{n}\, d\Gamma_t + \int_{\widetilde{\Gamma}_t^{\text{endo}}} p\mathbf{n}\, d\Gamma_t,$$

which entails:

$$\int_{\Gamma_t^{\text{base}}} \mathbf{T}\mathbf{n}\, d\Gamma_t = - \int_{\widetilde{\Gamma}_t^{\text{base}}} \mathbf{T}\mathbf{n}\, d\Gamma_t = \int_{\Gamma_t^{\text{endo}}} p\mathbf{n}\, d\Gamma_t = \int_{\Gamma_0^{\text{endo}}} p\, J\mathbf{F}^{-T}\mathbf{n}\, d\Gamma_0. \tag{17}$$

Eq. (17) allows to derive the total stress applied on the boundary Γ_t^{base}, but not its pointwise distribution. This is the price to pay as we do not explicitly include the domain $\widetilde{\Omega}_t$ into the EM model. Nonetheless, if we assume that the stress is uniformly distributed, we get:

$$\mathbf{T}\mathbf{n} = |\Gamma_t^{\text{base}}|^{-1} \int_{\Gamma_0^{\text{endo}}} p\, J\mathbf{F}^{-T}\mathbf{n}\, d\Gamma_0 \qquad \text{on } \Gamma_t^{\text{base}}, \tag{18}$$

which reads, in the reference configuration:

$$\mathbf{P}\mathbf{N} = \frac{\|J\mathbf{F}^{-T}\mathbf{N}\|}{\int_{\Gamma_0^{\text{base}}} \|J\mathbf{F}^{-T}\mathbf{N}\| d\Gamma_0} \int_{\Gamma_0^{\text{endo}}} pJ\mathbf{F}^{-T}\mathbf{N} d\Gamma_0 \qquad \text{on } \Gamma_0^{\text{base}}. \tag{19}$$

We notice that thanks to Eq. (19) the net force exerted by the fluid on the solid is null since the stress on Γ_0^{base} perfectly balances the stress exerted on Γ_0^{endo}. This is coherent with the hydrostatic nature of the pressure force, which contributes to the energy of the system, but not to its momentum.

To further validate the consistency of the newly introduced boundary condition (19), we consider the energetic balance of the LV. With this purpose, we multiply the first equation of Eq. (13) by $\frac{\partial \mathbf{d}}{\partial t}$ and we integrate over Ω_0, getting:

$$\int_{\Omega_0} \rho \frac{\partial^2 \mathbf{d}}{\partial t^2} \cdot \frac{\partial \mathbf{d}}{\partial t}\, d\mathbf{X} + \int_{\Omega_0} \mathbf{P}(\mathbf{d}) \colon \nabla \frac{\partial \mathbf{d}}{\partial t}\, d\mathbf{X} - \int_{\partial \Omega_0} \mathbf{P}(\mathbf{d})\mathbf{N} \cdot \frac{\partial \mathbf{d}}{\partial t}\, d\Gamma_0 = 0. \tag{20}$$

The first term of Eq. (20) provides the time derivative of the kinetic energy, defined as $\mathcal{K}(t) = \int_{\Omega_0} \rho \left| \frac{\partial \mathbf{d}}{\partial t} \right|^2 d\mathbf{X}$. By recalling the additive splitting of the Piola tensor as $\mathbf{P} = \mathbf{P}^{\text{pass}} + \mathbf{P}^{\text{act}}$, the second term of Eq. (20) gives rise to two terms, namely:

- $\int_{\Omega_0} \frac{\partial \mathcal{W}}{\partial \mathbf{F}} \colon \nabla \frac{\partial \mathbf{d}}{\partial t}\, d\mathbf{X} = \frac{d}{dt} \int_{\Omega_0} \mathcal{W}(\mathbf{F})\, d\mathbf{X}$, the time derivative of the total hyperelastic energy;
- $\Pi^{\text{act}}(t) = \int_{\Omega_0} \mathbf{P}^{\text{act}} \colon \nabla \frac{\partial \mathbf{d}}{\partial t}\, d\mathbf{X}$, the total power produced by the microscopic active tension in the considered ventricular tissue.

Finally, in the last term of Eq. (20) we replace, in each part of the boundary $\partial \Omega_0$, the term $\mathbf{P}(\mathbf{d})\mathbf{N}$ by the associated boundary conditions, according to Eq. (13). In conclusion, we obtain the following balance:

$$\frac{d\mathcal{K}(t)}{dt} + \frac{d\mathcal{E}(t)}{dt} + \Pi^{\text{act}}(t) + \Pi^{\text{press}}(t) + \Pi^{\text{diss}}(t) = 0, \qquad \forall t \in (0, T], \tag{21}$$

where we have defined the total elastic energy as the sum of the volumetric hyperelastic energy and the energy stored by the pericardium:

$$\mathcal{E}(t) = \int_{\Omega_0} \mathcal{W}(\mathbf{F})\, d\mathbf{X} + \frac{1}{2} \int_{\Gamma_0^{\text{epi}}} \left[K_\perp^{\text{epi}} \|\mathbf{d} \cdot \mathbf{N}\|^2 + K_\parallel^{\text{epi}} \|(\mathbf{I} - \mathbf{N} \otimes \mathbf{N})\, \mathbf{d}\|^2 \right] d\Gamma_0.$$

Conversely, the following nonnegative term corresponds to the power dissipated by viscous interaction with the pericardium:

$$\Pi^{\text{diss}}(t) = \int_{\Gamma_0^{\text{endo}}} \left[C_\perp^{\text{epi}} \left\| \frac{\partial \mathbf{d}}{\partial t} \cdot \mathbf{N} \right\|^2 + C_\parallel^{\text{epi}} \left\| (\mathbf{I} - \mathbf{N} \otimes \mathbf{N}) \frac{\partial \mathbf{d}}{\partial t} \right\|^2 \right] d\Gamma_0 \geq 0.$$

Finally, the following term represents the power exerted by the blood in the ventricular cavity through the pressure $p(t)$:

$$\begin{aligned} &\Pi^{\text{press}}(t) \\ &= p(t) \left[\int_{\Gamma_0^{\text{endo}}} J\mathbf{F}^{-T}\mathbf{N} \cdot \frac{\partial \mathbf{d}}{\partial t}\, d\Gamma_0 - \frac{\int_{\Gamma_0^{\text{base}}} \|J\mathbf{F}^{-T}\mathbf{N}\| \frac{\partial \mathbf{d}}{\partial t}\, d\Gamma_0}{\int_{\Gamma_0^{\text{base}}} \|J\mathbf{F}^{-T}\mathbf{N}\| d\Gamma_0} \cdot \int_{\Gamma_0^{\text{endo}}} J\mathbf{F}^{-T}\mathbf{N} d\Gamma_0 \right]. \end{aligned} \tag{22}$$

We now check that the value of $\Pi^{\text{press}}(t)$ of Eq. (22), derived from the boundary condition (19), is consistent with the formula $\Pi^{\text{press}}(t) = p(t)\frac{dV(t)}{dt}$, corresponding the power exerted by the pressure $p(t)$ inside a cavity with volume $V(t)$ [107]. With this aim, we compute the time derivative of the volume enclosed by the considered domain, given by:

$$\frac{dV(t)}{dt} = \frac{d}{dt} \int_{\Omega_t^{\text{fluid}}} 1\, d\mathbf{x} = \int_{\Gamma_t^{\text{endo}}} \frac{\partial \mathbf{d}}{\partial t} \cdot \mathbf{N}\, d\mathbf{x} + \int_{\Gamma_t^{\text{cap}}} \frac{\partial \mathbf{d}}{\partial t} \cdot \mathbf{N}\, d\mathbf{x}, \tag{23}$$

where we have used the Reynolds transport theorem [108]. With Γ_t^{cap} we denote the surface enclosed by the orifice ring. Since its motion is not directly tracked by the variables of problem (16), we estimate it by the motion of the ventricular base. Specifically, we assume that the velocity on Γ_t^{cap} is equal to the integral mean velocity on Γ_t^{base}:

$$\left. \frac{\partial \mathbf{d}}{\partial t} \right|_{\Gamma_t^{\text{cap}}} \simeq |\Gamma_t^{\text{base}}|^{-1} \int_{\Gamma_t^{\text{base}}} \frac{\partial \mathbf{d}}{\partial t}\, d\Gamma_t = \frac{\int_{\Gamma_0^{\text{base}}} \|J\mathbf{F}^{-T}\mathbf{N}\| \frac{\partial \mathbf{d}}{\partial t}\, d\Gamma_0}{\int_{\Gamma_0^{\text{base}}} \|J\mathbf{F}^{-T}\mathbf{N}\| d\Gamma_0}. \tag{24}$$

Moreover, by the divergence theorem [107], we have:

$$\int_{\Gamma_t^{\text{cap}}} \mathbf{N}\, d\mathbf{x} = - \int_{\Gamma_t^{\text{endo}}} \mathbf{N}\, d\mathbf{x} = - \int_{\Gamma_0^{\text{endo}}} J\mathbf{F}^{-T}\mathbf{N} d\Gamma_0. \tag{25}$$

Finally, by combining Eqs. (22)–(25), we get $\Pi^{\mathrm{press}}(t) = p(t)\frac{dV(t)}{dt}$. This further confirms the validity of the boundary condition of Eq. (19). Moreover, we notice that in case of motion given by a rigid translation (i.e. $\frac{\partial \mathbf{d}}{\partial t}$ constant in space), the two terms in Eq. (22) cancel, giving $\Pi^{\mathrm{press}}(t) = 0$. This property, which is not satisfied if e.g. homogeneous Neumann boundary conditions are applied on Γ_0^{base}, provides a further verification of Eq. (19). For these reasons, we call Eq. (19) *energy-consistent boundary condition.*

Appendix D. Error estimation of ANN-EM vs. HF-EM in 1D

To gain some insight on the effect of the feedback of mechanics on activation, we consider a one-dimensional steady-state version of Eq. (13), which can be regarded as a simple model for the tissue deformation along the direction of the active force (i.e. the fibers direction). By denoting by d the one-dimensional displacement and by $e = \frac{d}{dx}d$ the one-dimensional strain, we consider an elastic energy $\mathcal{W}(e)$ and we define the passive stress as $P^{\mathrm{pass}}(e) := \mathcal{W}'(e)$, while we denote by P^{act} the active stress. The mechanical equilibrium equation in the domain $(0, L)$ reads as follows:

$$\begin{cases} -\dfrac{d}{dx}\left(P^{\mathrm{pass}}\left(\dfrac{d}{dx}d(x)\right) + P^{\mathrm{act}}(x)\right) = 0 \quad \text{for } x \in (0, L) \\ d(0) = 0 \\ P(\frac{d}{dx}d(L)) + P^{\mathrm{act}}(L) = p, \end{cases} \tag{26}$$

where we set a symmetry boundary condition at one side and a load p at the other side. Coherently with model (1), the active stress is a function of calcium concentration and sarcomere length: $P^{\mathrm{act}}(x) = T_a([\mathrm{Ca}^{2+}]_{\mathrm{i}}(x), SL(x)) = T_a([\mathrm{Ca}^{2+}]_{\mathrm{i}}(x), SL_0(1 + e(x)))$. The solution of Eq. (26) satisfies:

$$P^{\mathrm{pass}}(e(x)) + T_a([\mathrm{Ca}^{2+}]_{\mathrm{i}}(x), SL_0(1 + e(x))) = p \quad \forall x \in (0, L)$$

Consider now a perturbed version of Eq. (26), where the function T_a is replaced by a surrogate $\widetilde{T_a} = T_a + \eta$, affected by the error η (in our case, η can be regarded as the approximation error associated with the reduced ANN model). By asymptotic analysis, the perturbed solution $\tilde{d}$ satisfies:

$$\frac{d}{dx}\tilde{d} - \frac{d}{dx}d \sim \eta \left(\frac{\partial T_a}{\partial SL} SL_0 + \mathcal{W}''(e)\right)^{-1}.$$

Hence, the active stress in the perturbed problem is linked with the HF one by:

$$\widetilde{T_a}([\mathrm{Ca}^{2+}]_{\mathrm{i}}, SL_0(1 + \tilde{e}(x))) - T_a([\mathrm{Ca}^{2+}]_{\mathrm{i}}, SL_0(1 + e(x))) \sim \eta \left(1 + \frac{\frac{\partial T_a}{\partial SL} SL_0}{\mathcal{W}''(e)}\right)^{-1}.$$

Being the elastic energy convex, the term $\mathcal{W}''(e)$ is positive. Thus, on the ascending limb of the force–length relationship ($\frac{\partial T_a}{\partial SL} > 0$), the error η is attenuated; conversely, on the descending limb ($\frac{\partial T_a}{\partial SL} < 0$) it is amplified.

References

[1] A. Quarteroni, T. Lassila, S. Rossi, R. Ruiz-Baier, Integrated heart–coupling multiscale and multiphysics models for the simulation of the cardiac function, Comput. Methods Appl. Mech. Engrg. 314 (2017) 345–407.

[2] M. Fink, S. Niederer, E. Cherry, F. Fenton, J. Koivumäki, G. Seemann, R. Thul, H. Zhang, F. Sachse, D. Beard, E. Crampin, N. Smith, Cardiac cell modelling: observations from the heart of the cardiac physiome project, Prog. Biophys. Mol. Biol. 104 (1) (2011) 2–21.

[3] D. Nordsletten, S. Niederer, M. Nash, P. Hunter, N. Smith, Coupling multi-physics models to cardiac mechanics, Prog. Biophys. Mol. Biol. 104 (1–3) (2011) 77–88.

[4] L. Glass, P. Hunter, A. McCulloch, Theory of Heart: Biomechanics, Biophysics, and Nonlinear Dynamics of Cardiac Function, Springer Science & Business Media, 2012.

[5] M. Caruel, R. Chabiniok, P. Moireau, Y. Lecarpentier, D. Chapelle, Dimensional reductions of a cardiac model for effective validation and calibration, Biomech. Model. Mechanobiol. 13 (4) (2014) 897–914.

[6] A. Quarteroni, L. Dede', A. Manzoni, C. Vergara, Mathematical Modelling of the Human Cardiovascular System: Data, Numerical Approximation, Clinical Applications, in: Cambridge Monographs on Applied and Computational Mathematics, Cambridge University Press, 2019.

[7] R. Chabiniok, V. Wang, M. Hadjicharalambous, L. Asner, J. Lee, M. Sermesant, E. Kuhl, A. Young, P. Moireau, M. Nash, D. Chapelle, D. Nordsletten, Multiphysics and multiscale modelling, data–model fusion and integration of organ physiology in the clinic: ventricular cardiac mechanics, Interface Focus 6 (2) (2016) 20150083.

[8] N. Smith, D. Nickerson, E. Crampin, P. Hunter, Multiscale computational modelling of the heart, Acta Numer. 13 (2004) 371–431.
[9] E.J. Crampin, M. Halstead, P. Hunter, P. Nielsen, D. Noble, N. Smith, M. Tawhai, Computational physiology and the physiome project, Exp. Physiol. 89 (1) (2004) 1–26.
[10] J. Rice, G. Stolovitzky, Y. Tu, P. de Tombe, Ising model of cardiac thin filament activation with nearest-neighbor cooperative interactions, Biophys. J. 84 (2) (2003) 897–909.
[11] J. Rice, P. de Tombe, Approaches to modeling crossbridges and calcium-dependent activation in cardiac muscle, Prog. Biophys. Mol. Biol. 85 (2) (2004) 179–195.
[12] T. Washio, J. Okada, S. Sugiura, T. Hisada, Approximation for cooperative interactions of a spatially-detailed cardiac sarcomere model, Cell. Mol. Bioeng. 5 (1) (2012) 113–126.
[13] F. Regazzoni, L. Dedè, A. Quarteroni, Machine learning for fast and reliable solution of time-dependent differential equations, J. Comput. Phys. (ISSN: 0021-9991) 397 (2019) 108852.
[14] F. Regazzoni, L. Dedè, A. Quarteroni, Active contraction of cardiac cells: a reduced model for sarcomere dynamics with cooperative interactions, Biomech. Model. Mechanobiol. (2018) 1–24.
[15] A.M. Katz, Physiology of the Heart, Lippincott Williams & Wilkins, 2010.
[16] D. Bers, Excitation-Contraction Coupling and Cardiac Contractile Force, Vol. 237, Springer Science & Business Media, 2001.
[17] G.J. Tortora, B.H. Derrickson, Principles of Anatomy and Physiology, John Wiley & Sons, 2008.
[18] G.W. Jenkins, C.P. Kemnitz, G.J. Tortora, Anatomy and Physiology: from Science to Life, Wiley Hoboken, 2007.
[19] M. Caruel, L. Truskinovsky, Physics of muscle contraction, Rep. Progr. Phys. 81 (3) (2018) 036602.
[20] F. Regazzoni, L. Dedè, A. Quarteroni, Active force generation in cardiac muscle cells: mathematical modeling and numerical simulation of the actin-myosin interaction, Vietnam J. Math. (2020).
[21] A. Landesberg, S. Sideman, Coupling calcium binding to troponin c and cross-bridge cycling in skinned cardiac cells, Amer. J. Physiol.-Heart Circ. Physiol. 266 (3) (1994) H1260–H1271.
[22] M. Razumova, A. Bukatina, K. Campbell, Stiffness-distortion sarcomere model for muscle simulation, J. Appl. Physiol. 87 (5) (1999) 1861–1876.
[23] J. Rice, R. Winslow, W. Hunter, Comparison of putative cooperative mechanisms in cardiac muscle: length dependence and dynamic responses, Amer. J. Physiol.-Heart Circ. Physiol. 276 (5) (1999) H1734–H1754.
[24] F. Sachse, K. Glänzel, G. Seemann, Modeling of protein interactions involved in cardiac tension development, Int. J. Bifurcation Chaos 13 (12) (2003) 3561–3578.
[25] J. Kentish, H. ter Keurs, L. Ricciardi, J. Bucx, M. Noble, Comparison between the sarcomere length-force relations of intact and skinned trabeculae from rat right ventricle. influence of calcium concentrations on these relations., Circ. Res. 58 (6) (1986) 755–768.
[26] D. Dobesh, J. Konhilas, P. de Tombe, Cooperative activation in cardiac muscle: impact of sarcomere length, Amer. J. Physiol.-Heart Circ. Physiol. 51 (3) (2002) H1055.
[27] H. Ter Keurs, E. Hollander, M. ter Keurs, The Effect of Sarcomere Length on the Force–Cytosolic [Ca2+] Relationship in Intact Rat Cardiac Trabeculae, Skeletal Muscle Mechanics: from Mechanics to Function, Wiley, New York, 2000, pp. 53–70.
[28] H. Ter Keurs, T. Shinozaki, Y. Zhang, M. Zhang, Y. Wakayama, Y. Sugai, Y. Kagaya, M. Miura, P. Boyden, B. Stuyvers, et al., Sarcomere mechanics in uniform and non-uniform cardiac muscle: a link between pump function and arrhythmias, Prog. Biophys. Mol. Biol. 97 (2–3) (2008) 312–331.
[29] J. Hussan, P. de Tombe, J. Rice, A spatially detailed myofilament model as a basis for large-scale biological simulations, IBM J. Res. Dev. 50 (6) (2006) 583–600.
[30] T. Washio, J. Okada, A. Takahashi, K. Yoneda, Y. Kadooka, S. Sugiura, T. Hisada, Multiscale heart simulation with cooperative stochastic cross-bridge dynamics and cellular structures, Multiscale Model. Simul. 11 (4) (2013) 965–999.
[31] T. Washio, K. Yoneda, J. Okada, T. Kariya, S. Sugiura, T. Hisada, Ventricular fiber optimization utilizing the branching structure, Int. J. Numer. Methods Biomed. Eng. (2015).
[32] P. Hunter, A. McCulloch, H. Ter Keurs, Modelling the mechanical properties of cardiac muscle, Prog. Biophys. Mol. Biol. 69 (2) (1998) 289–331.
[33] S.A. Niederer, P.J. Hunter, N.P. Smith, A quantitative analysis of cardiac myocyte relaxation: a simulation study, Biophys. J. 90 (5) (2006) 1697–1722.
[34] J. Rice, F. Wang, D. Bers, P. de Tombe, Approximate model of cooperative activation and crossbridge cycling in cardiac muscle using ordinary differential equations, Biophys. J. 95 (5) (2008) 2368–2390.
[35] S. Land, S.A. Niederer, J.M. Aronsen, E.K. Espe, L. Zhang, W.E. Louch, I. Sjaastad, O.M. Sejersted, N.P. Smith, An analysis of deformation-dependent electromechanical coupling in the mouse heart, J. Physiol. 590 (18) (2012) 4553–4569.
[36] S. Land, S. Park-Holohan, N. Smith, C. dos Remedios, J. Kentish, S. Niederer, A model of cardiac contraction based on novel measurements of tension development in human cardiomyocytes, J. Mol. Cell. Cardiol. 106 (2017) 68–83.
[37] S. Campbell, F. Lionetti, K. Campbell, A. McCulloch, Coupling of adjacent tropomyosins enhances cross-bridge-mediated cooperative activation in a Markov model of the cardiac thin filament, Biophys. J. 98 (10) (2010) 2254–2264.
[38] S. Land, S. Niederer, A spatially detailed model of isometric contraction based on competitive binding of troponin i explains cooperative interactions between tropomyosin and crossbridges, PLoS Comput. Biol. 11 (8) (2015) e1004376.
[39] A.C. Antoulas, D.C. Sorensen, S. Gugercin, A Survey of Model Reduction Methods for Large-Scale Systems, Tech. rep., Virginia Tech, 2000.
[40] P. Benner, V. Mehrmann, D.C. Sorensen, Dimension Reduction of Large-Scale Systems, Vol. 35, Springer, 2005.
[41] A. Quarteroni, A. Manzoni, F. Negri, Reduced Basis Methods for Partial Differential Equations: An Introduction, Vol. 92, Springer, 2015.

[42] P. Benner, S. Gugercin, K. Willcox, A survey of projection-based model reduction methods for parametric dynamical systems, SIAM Rev. 57 (4) (2015) 483–531.

[43] A.C. Antoulas, Approximation of Large-Scale Dynamical Systems, Vol. 6, Siam, 2005.

[44] Z. Bai, Krylov subspace techniques for reduced-order modeling of large-scale dynamical systems, Appl. Numer. Math. 43 (1–2) (2002) 9–44.

[45] U. Baur, C. Beattie, P. Benner, S. Gugercin, Interpolatory projection methods for parameterized model reduction, SIAM J. Sci. Comput. 33 (5) (2011) 2489–2518.

[46] R.W. Freund, Model reduction methods based on krylov subspaces, Acta Numer. 12 (2003) 267–319.

[47] B. Moore, Principal component analysis in linear systems: Controllability, observability, and model reduction, IEEE Trans. Autom. Control 26 (1) (1981) 17–32.

[48] J.S. Hesthaven, G. Rozza, B. Stamm, Certified Reduced Basis Methods for Parametrized Partial Differential Equations, Springer, 2016.

[49] J.P. Fink, W. Rheinboldt, On the error behavior of the reduced basis technique for nonlinear finite element approximations, ZAMM-J. Appl. Math. Mech./Z. Angew. Math. Mech. 63 (1) (1983) 21–28.

[50] J.S. Peterson, The reduced basis method for incompressible viscous flow calculations, SIAM J. Sci. Stat. Comput. 10 (4) (1989) 777–786.

[51] C. Prud'Homme, D.V. Rovas, K. Veroy, L. Machiels, Y. Maday, A.T. Patera, G. Turinici, Reliable real-time solution of parametrized partial differential equations: Reduced-basis output bound methods, J. Fluids Eng. 124 (1) (2002) 70–80.

[52] F. Negri, A. Manzoni, D. Amsallem, Efficient model reduction of parametrized systems by matrix discrete empirical interpolation, J. Comput. Phys. 303 (2015) 431–454.

[53] Y. Maday, N.C. Nguyen, A.T. Patera, S. Pau, A general multipurpose interpolation procedure: the magic points, Commun. Pure Appl. Anal. 8 (1) (2009) 383.

[54] S. Chaturantabut, D.C. Sorensen, Nonlinear model reduction via discrete empirical interpolation, SIAM J. Sci. Comput. 32 (5) (2010) 2737–2764.

[55] M. Drohmann, B. Haasdonk, M. Ohlberger, Reduced basis approximation for nonlinear parametrized evolution equations based on empirical operator interpolation, SIAM J. Sci. Comput. 34 (2) (2012) A937–A969.

[56] K. Löwner, Über Monotone matrixfunktionen, Math. Z. 38 (1) (1934) 177–216.

[57] A. Mayo, A. Antoulas, A framework for the solution of the generalized realization problem, Linear Algebra Appl. 425 (2–3) (2007) 634–662.

[58] S. Lefteriu, A.C. Antoulas, A new approach to modeling multiport systems from frequency-domain data, IEEE Trans. Comput.-Aided Des. Integr. Circuits Syst. 29 (1) (2010) 14–27.

[59] D. Deschrijver, T. Dhaene, Rational modeling of spectral data using orthonormal vector fitting, in: 9th IEEE Workshop on Signal Propagation on Interconnects, 2005, pp. 111–114.

[60] D. Deschrijver, B. Haegeman, T. Dhaene, Orthonormal vector fitting: A robust macromodeling tool for rational approximation of frequency domain responses, IEEE Trans. Adv. Packag. 30 (2) (2007) 216–225.

[61] A.F. Hernandez, M.G. Gallivan, An exploratory study of discrete time state-space models using kriging, in: American Control Conference, 2008, IEEE, 2008, pp. 3993–3998.

[62] C.E. Rasmussen, Gaussian processes in machine learning, in: Advanced Lectures on Machine Learning, Springer, 2004, pp. 63–71.

[63] A. Menafoglio, P. Secchi, M. Dalla Rosa, A universal kriging predictor for spatially dependent functional data of a hilbert space, Electron. J. Stat. 7 (2013) 2209–2240.

[64] S.L. Brunton, J.L. Proctor, J.N. Kutz, Discovering governing equations from data by sparse identification of nonlinear dynamical systems, Proc. Natl. Acad. Sci. (2016) 201517384.

[65] A.C. Antoulas, I.V. Gosea, A.C. Ionita, Model reduction of bilinear systems in the loewner framework, SIAM J. Sci. Comput. 38 (5) (2016) B889–B916.

[66] I.V. Gosea, A.C. Antoulas, Model reduction of linear and nonlinear systems in the loewner framework: A summary, in: Control Conference (ECC), 2015 European, IEEE, 2015, pp. 345–349.

[67] C. Gu, QLMOR: A projection-based nonlinear model order reduction approach using quadratic-linear representation of nonlinear systems, IEEE Trans. Comput.-Aided Des. Integr. Circuits Syst. 30 (9) (2011) 1307–1320.

[68] M. Raissi, P. Perdikaris, G.E. Karniadakis, Multistep neural networks for data-driven discovery of nonlinear dynamical systems, 2018, arXiv preprint arXiv:1801.01236.

[69] M. Guo, J.S. Hesthaven, Data-driven reduced order modeling for time-dependent problems, Comput. Methods Appl. Mech. Engrg. 345 (2019) 75–99.

[70] S. Fresca, L. Dede, A. Manzoni, A Comprehensive Deep Learning-Based Approach to Reduced Order Modeling of Nonlinear Time-Dependent Parametrized PDEs, MOX Report 2020/02, Politecnico di Milano, 2020.

[71] F. Regazzoni, Mathematical Modeling and Machine Learning for the Numerical Simulation of Cardiac Electromechanics (Ph.D. thesis), Politecnico di Milano, 2020.

[72] J. Keener, J. Sneyd, Mathematical Physiology, Vol. 1, Springer, 2009.

[73] D. Chapelle, P. Le Tallec, P. Moireau, M. Sorine, Energy-preserving muscle tissue model: formulation and compatible discretizations, Int. J. Multiscale Comput. Eng. 10 (2) (2012).

[74] M. Caruel, P. Moireau, D. Chapelle, Stochastic modeling of chemical–mechanical coupling in striated muscles, Biomech. Model. Mechanobiol. 18 (3) (2019) 563–587.

[75] F. Kimmig, D. Chapelle, P. Moireau, Thermodynamic properties of muscle contraction models and associated discrete-time principles, Adv. Model. Simul. Eng. Sci. 6 (1) (2019) 6.

[76] G. Cybenko, Approximation by superpositions of a sigmoidal function, Math. Control Signals Systems 2 (4) (1989) 303–314.
[77] J.W. Siegel, J. Xu, On the approximation properties of neural networks, 2019, arXiv preprint arXiv:1904.02311.
[78] J. He, L. Li, J. Xu, C. Zheng, Relu deep neural networks and linear finite elements, 2018, arXiv preprint arXiv:1807.03973.
[79] B. Yegnanarayana, Artificial Neural Networks, PHI Learning Pvt. Ltd., 2009.
[80] J. Nocedal, S. Wright, Numerical Optimization, second ed., Springer Science & Business Media, New York, NY, USA, 2006.
[81] A. Quarteroni, R. Sacco, F. Saleri, Numerical Mathematics, Vol. 37, Springer Science & Business Media, 2010.
[82] P. Janssen, W. Hunter, Force, not sarcomere length, correlates with prolongation of isosarcometric contraction, Amer. J. Physiol. - Heart Circ. Physiol. 269 (2) (1995) H676–H685.
[83] L. Dobrunz, P. Backx, D. Yue, Steady-state [Ca2+]i-force relationship in intact twitching cardiac muscle: direct evidence for modulation by isoproterenol and emd 53998, Biophys. J. 69 (1) (1995) 189–201.
[84] L. Ford, A. Huxley, R. Simmons, Tension responses to sudden length change in stimulated frog muscle fibres near slack length, J. Physiol. 269 (2) (1977) 441–515.
[85] P. de Tombe, G. Stienen, Impact of temperature on cross-bridge cycling kinetics in rat myocardium, J. Physiol. 584 (2) (2007) 591–600.
[86] A. Araujo, J. Walker, Kinetics of tension development in skinned cardiac myocytes measured by photorelease of Ca2+, Amer. J. Physiol. - Heart Circ. Physiol. 267 (5) (1994) H1643–H1653.
[87] M. Wolff, K. McDonald, R. Moss, Rate of tension development in cardiac muscle varies with level of activator calcium, Circ. Res. 76 (1) (1995) 154–160.
[88] P. Janssen, P. de Tombe, Uncontrolled sarcomere shortening increases intracellular Ca2+ transient in rat cardiac trabeculae, Amer. J. Physiol. - Heart Circ. Physiol. (ISSN: 0363-6135) 272 (4) (1997) H1892–H1897.
[89] A. Gerbi, L. Dedè, A. Quarteroni, A monolithic algorithm for the simulation of cardiac electromechanics in the human left ventricle, Math. Eng. 1 (1) (2018) 1–37.
[90] P. Colli Franzone, L.F. Pavarino, G. Savaré, Computational electrocardiology: mathematical and numerical modeling, in: Complex Systems in Biomedicine, Springer, 2006, pp. 187–241.
[91] P. Colli Franzone, L.F. Pavarino, S. Scacchi, Mathematical Cardiac Electrophysiology, Vol. 13, Springer, 2014.
[92] K.H. Ten Tusscher, A.V. Panfilov, Alternans and spiral breakup in a human ventricular tissue model, Amer. J. Physiol. - Heart Circ. Physiol. 291 (3) (2006) H1088–H1100.
[93] R.W. Ogden, Non-linear Elastic Deformations, Courier Corporation, 1997.
[94] G. Giantesio, A. Musesti, D. Riccobelli, A comparison between active strain and active stress in transversely isotropic hyperelastic materials, J. Elasticity (2019) 1–20.
[95] T.P. Usyk, I.J. LeGrice, A.D. McCulloch, Computational model of three-dimensional cardiac electromechanics, Comput. Vis. Sci. 4 (4) (2002) 249–257.
[96] M.R. Pfaller, J.M. Hörmann, M. Weigl, A. Nagler, R. Chabiniok, C. Bertoglio, W.A. Wall, The importance of the pericardium for cardiac biomechanics: From physiology to computational modeling, Biomech. Model. Mechanobiol. 18 (2) (2019) 503–529.
[97] N. Westerhof, J.-W. Lankhaar, B.E. Westerhof, The arterial Windkessel, Med. Biol. Eng. Comput. 47 (2) (2009) 131–141.
[98] A. Gerbi, L. Dedè, A. Quarteroni, Segregated Algorithms for the Numerical Simulation of Cardiac Electromechanics in the Left Human Ventricle, MOX Report 2018/28, Politecnico di Milano, 2018.
[99] M. Benzi, G.H. Golub, J. Liesen, Numerical solution of saddle point problems, Acta Numer. 14 (2005) 1–137.
[100] A. Gerbi, Numerical Approximation of Cardiac Electro-fluid-mechanical Models: Coupling Strategies for Large-scale Simulation (Ph.D. thesis), Ecole Polytechnique Fédérale de Lausanne, 2018.
[101] Zygote 3D models, https://www.zygote.com/.
[102] J.D. Bayer, R.C. Blake, G. Plank, N.A. Trayanova, A novel rule-based algorithm for assigning myocardial fiber orientation to computational heart models, Ann. Biomed. Eng. 40 (10) (2012) 2243–2254.
[103] S.S. Haykin, Neural Networks and Learning Machines, Vol. 3, Pearson Upper Saddle River, 2009.
[104] Y. LeCun, Y. Bengio, G. Hinton, Deep Learning, Nature 521 (7553) (2015) 436.
[105] J. Kaipio, E. Somersalo, Statistical and Computational Inverse Problems, Vol. 160, Springer Science & Business Media, 2006.
[106] F. Regazzoni, model-learning, https://github.com/FrancescoRegazzoni/model-learning.
[107] M.E. Gurtin, E. Fried, L. Anand, The Mechanics and Thermodynamics of Continua, Cambridge University Press, 2010.
[108] M.E. Gurtin, An Introduction to Continuum Mechanics, Vol. 158, Academic press, 1982.